Systematic corrections in Bragg xray diffraction of flat and curved crystals

C. T. Chantler and R. D. Deslattes

Related Articles

Note: Continuing improvements on the novel flat-response x-ray detector
Rev. Sci. Instrum. 82, 106106 (2011)

A combined small- and wide-angle x-ray scattering detector for measurements on reactive systems
Rev. Sci. Instrum. 82, 083104 (2011)

Compact and high-quality gamma-ray source applied to 10 m-range resolution radiography
Appl. Phys. Lett. 98, 264101 (2011)

A new white beam x-ray microdiffraction setup on the BM32 beamline at the European Synchrotron Radiation Facility
Rev. Sci. Instrum. 82, 033908 (2011)

Standard design for National Ignition Facility x-ray streak and framing cameras
Rev. Sci. Instrum. 81, 10E530 (2010)

Additional information on Rev. Sci. Instrum.

Journal Homepage: http://rsi.aip.org

Journal Information: http://rsi.aip.org/about/about_the_journal

Top downloads: http://rsi.aip.org/features/most_downloaded

Information for Authors: http://rsi.aip.org/authors

REVIEW ARTICLE

Systematic corrections in Bragg x-ray diffraction of flat and curved crystals

C. T. Chantler

School of Physics, University of Melbourne, Parkville, Victoria 3052, Australia

R. D. Deslattes

Quantum Metrology Division, National Institute of Standards and Technology, Gaithersburg, Maryland 20899

Measurements of spectral wavelengths in Bragg diffraction from crystals often require refractive index corrections to allow a detailed comparison of experiment with theory. These corrections are typically 100–300 ppm in the x-ray regime, and simple estimates may sometimes be accurate to 5% or better. The inadequacies of these estimates are discussed. Even with a possibly improved index of refraction estimate, this correction is insufficient since additional systematics in the diffraction process occur at or above this level. For example, asymmetries of diffraction profiles with π-polarized radiation or due to three-beam diffraction can approach the magnitude of refractive index corrections for flat or curved crystals. The depth of penetration of the x-ray field inside curved crystals, the shift of the mean angle to the diffracting planes, and lateral shifts around the crystal surface are rarely considered but can dominate over refractive index corrections, particularly for high-order diffraction or medium-energy x rays. Shifts and nonlinearities arise when diffracting surfaces lie off the Rowland circle, and exhibit strong and rapidly varying angular dependencies. Johann geometries with the source located on the Rowland circle should be avoided to minimize profile truncation shifts from crystal ranges or minimum grazing angles, and to avoid extreme scaling corrections. Other significant shifts are identified and illustrated, with functional relations provided to allow an estimation of related magnitudes. The central concerns of this paper are the effects on flat crystal diffraction and curved crystal diffraction in the Johann geometry, with a source and crystal of variable dimensions and location. Experiments often interpolate or extrapolate from calibration lines, so dependencies upon the diffracting angle are as important as the magnitude of the corrections. These dependencies are presented in formulas and graphs. © *1995 American Institute of Physics.*

I. INTRODUCTION

X-ray spectroscopy was developed after the discovery of x rays in 1895 by Röntgen and the observation of their diffraction by crystals by von Laue in 1912.[1,2] The wavelength dependence of the diffracting angle, and hence the possibility of the spectroscopy of x rays, was demonstrated by Bragg in 1913.[3,4]

The crystal diffraction of x rays continues to yield the highest resolution spectra in the x-ray regime, compared to solid state and other detector technologies. The intrinsic flat crystal resolving power can exceed $\lambda/\delta\lambda = 100\,000$ for single- or double-crystal combinations in particular perfect crystal diffracting planes of various crystals.[5] Experimental arrangements with resolving powers of 1000–10 000 are common across the x-ray range of energies. The realized spectral resolving powers are often limited by natural or other source widths, by (imaging) detector resolutions, or by geometric defocusing, rather than by the diffraction width.

With this high potential resolution and a high peak diffracting efficiency (approaching unity), the technique of crystal x-ray diffraction has proliferated in crystallographic studies, standard source calibration and measurements, synchrotron radiation monochromatization, atomic physics tests, and general experiments using accelerators, tokamaks, and electron beam ion traps. This high resolution also enables absolute measurements of the source profiles or wavelengths to below the part per million level (ppm or $\delta\lambda/\lambda = 10^{-6}$). However, this precision also requires the consideration of systematics at this level.

X-ray diffraction theory has been developed by Darwin, Ewald, Prins, Zachariasen, James, and others.[6–11] Modeling procedures for flat and curved crystal calculations have existed for some time.[12] Most are designed for reflectivity or profile shape determinations and neglect systematic shifts of the Bragg peaks. Estimates of such shifts often derive from the Bragg relation inside the crystal as compared to *in vacuo* (that is, with and without refraction) and involve significant approximations.[13,14] Although it is well known that the application of these equations is approximate, the nature and magnitude of these approximations are often poorly understood or neglected.

These estimates are widely used by researchers using flat or curved crystal diffraction. One purpose of this paper is to indicate the range of validity of generally used approximations as compared to precision dynamical diffraction theory, so that experimentalists will be more informed as to when and how detailed corrections should be implemented in practice. Our attention is restricted to Bragg (reflecting) x-ray

diffraction because it is the dominant and optimal form for low and medium energy x-ray diffraction. The paper is divided into three sections and numerous subsections.

Our intention is to simplify the complexity of these corrections in such a way as to invite researchers to pursue more critical measurements, without necessarily requiring the use of a long and computationally-intensive theory in situations where it is not needed. The effects are therefore related to common crystals used in the x-ray regime, with graphs provided for typical cases.

Section II is concerned with effects which have their origin in flat crystal diffraction. This includes the well-known refractive index correction and its various approximations. The section also discusses asymmetric diffraction and polarization dependencies, as well as multiple-beam interactions. These considerations also carry over to curved crystals. The principles discussed, primarily for single-crystal diffraction, also apply for instruments with multiple crystal elements in monolithic or separated forms.

Section III is concerned with a series of effects which often dominate for curved crystals while being generally negligible for flat crystals. Curved crystal corrections are less familiar to many researchers. The depth of penetration of the x-ray field inside curved crystals, the shift of the mean angle to diffracting planes, and lateral shifts around the crystal surface are addressed. Shifts and dispersion nonlinearities arising when diffracting surfaces lie off the Rowland circle are also a major consideration. Several of the effects are isolated and quantified here for the first time. The specific concern is with Bragg diffraction in the Johann geometry, although many of the relations are of general application.

Refractive index corrections occur at the level of 100–300 ppm and hence may be readily observed with modern instrumentation. However, other systematic contributions to profile centroid shift, detailed in this paper, can often exceed this level and are less well known. Researchers working with measurements approaching the ppm level will be concerned with estimating the magnitude of these effects in order to decide whether to evaluate or avoid them for the specific crystal, curvature, energy, and geometry. Experiments often involve interpolation or extrapolation from calibration lines, so that dependencies upon diffracting angle are as important as the magnitude of the corrections. These dependencies are presented in formulas and graphs.

II. FLAT CRYSTAL SYSTEMATIC CORRECTIONS

A. Overview

Common approximations for *refractive index corrections* are indicated in Sec. II B, which provides a brief review of the standard formulas. Section II C compares these forms across large ranges for selected crystals. This demonstrates the limitations of some commonly used equations. The accuracy of refractive index estimates can be limited by form factor uncertainties, in optimum cases, rather than by other approximations or effects.

Sections II D and II E indicate the main corrections to these prescriptions following (standard) two-beam dynamical diffraction. The first correction (*asymmetric diffraction*) is

well defined but depends on the orientation of diffracting planes in the crystal, which are sometimes inadequately known. The second correction (*peak profile asymmetry*) depends on the crystal thickness and perfection, as explained below. Asymmetries of diffraction profiles with π-polarized radiation (see Sec. II D), which generally occur for all crystals, can introduce major corrections to refractive index predictions, at the 10%–50% level, and are therefore important if high accuracy is required. This correction is well defined in standard two-beam dynamical diffraction, but is not given to convenient approximation. However, simple approximations are presented here in formulas and graphs.

Section II F indicates typical uncertainties relating to the use of databases as well as the results of crystal structure determinations. Sections II G–II I illustrate the complexity of real systems beyond two-beam diffraction in forbidden diffracting regimes or in local *three-beam interaction* regimes. Other significant but tertiary effects, including mosaicity and diffraction tail asymmetry, are discussed briefly in Sec. II J.

The scales of these contributions are illustrated in summary form in Table I, where it should be remembered that the relative magnitude of these effects can easily vary by an order of magnitude from one crystal type to another. Despite the overall complexity, high accuracy is certainly possible with curved or flat crystal measurements, either by explicit avoidance of problem regimes or by adequate correction for the systematics involved. Precision measurements can compare unknowns to a nearby calibration line, so only the difference in refractive index and other corrections is directly relevant. For example, the refractive index contribution to systematic corrections between lines separated by less than 2° in the same order of diffraction and away from near-normal incidence or any absorption edges is generally an order of magnitude smaller than the absolute correction.

This example of an appropriate experimental design can achieve a sensitivity of perhaps 20–30 ppm without requiring refractive index corrections. Further, if a series of calibration lines covers the region of the unknowns and is well distributed, the slope of the spectrometer dispersion can also be estimated, and under appropriate conditions only the consequent error in, or variation of, this slope will yield a systematic error. Typically, this can add an order of magnitude in accuracy. In both these cases, of course, the calibration lines must be measured on an absolute footing elsewhere or with respect to further calibration lines at a similar level of precision. Detailed discussion of how this could or should proceed has been given elsewhere, following primary optical standard and crystal lattice spacing determination and a comparison for the x-ray and γ-ray regimes.[15,16]

B. Refractive index shifts for perfect crystals in symmetric diffraction

Estimates of refractive index shifts derived from the Bragg relation inside the crystal compared to *in vacuo* usually follow the formula[13]

TABLE I. Magnitudes of corrections relative to refractive index shifts; Typical estimates for flat crystals.

Factor	Location	Percentage	Sec.
Use of Eqs. (3) and (4)	Near atomic absorption edge	3%–12%	II B and II C
	Far from edges	1%–2%	
	Medium-high Bragg angles	6%–19%	
Use of Eqs. (2) and (5b)	Generally	0.1%–0.2%	II B and II C
	High Bragg angles	1.0%	
Asymmetric diffraction, 1°	Angle to surface[a]	2%–7%	II D
	Exit vs incident angle	0.1%–1.0%	
Peak shift	Thick perfect crystal	10%–50%	II E
	Very thin or ideally mosaic crystal	0%	
Perfect crystal thickness ±10%[b]	Peak shift	1%–5%	II E
	Mean shift	0.1%–1.0%	
Form factor uncertainties	Generally	0.1%–1.0%	II F
Lattice coordinate error	Generally	<0.5%	II F
Possible three-beam interaction	Allowed, low order, high angle	0%	II H
	Allowed, low order, medium angle	1%–20%	II H
	Allowed, medium order	10%–200%	II I
	Forbidden	5%–100%	II G
Tail asymmetry	Extreme Bragg angles	5%–10%	II J

[a]After correction for α_p itself.
[b]Intermediate thickness regime.

$$\frac{n\lambda}{2d \sin \theta_C}=\left(1+\frac{(1+\mu_r)(\mu_r-1)}{\sin^2 \theta_C}\right)^{1/2} \simeq 1 - \frac{1-\mu_r}{\sin^2 \theta_C},$$ (1)

where λ is the incident (vacuum) wavelength of the radiation, d is the lattice spacing, n is the order of diffraction, μ_r is the refractive index, and θ_C is the "center" of the Bragg peak.[13] The Bragg angle θ_B follows from setting the right-hand side to unity, and a semiempirical correction to the angular location of diffraction follows from equating $\delta = 1 - \mu_r$ to, e.g.,

$$\delta = \frac{\lambda^2 r_0 F_0}{2\pi V},$$ (2)

where $r_0 = e^2/m_e c^2$, F_0 is the structure factor for forward scattering (hkl=000), and V is the unit cell volume. Considering energies well away from absorption edges, the expression may be simplified further using the effective electron number density

$$\frac{F_0}{V} \simeq n_e = \frac{N_A \rho Z_m}{M_w},$$ (3)

where N_A is Avogadro's number, ρ is the density of the crystal, Z_m is the number of electrons per molecule, and M_w is the molecular weight (convention is not followed, in order to avoid confusion with Z, electron mass, and refractive index). As opposed to visible light, the refractive index for x rays is usually less than unity, so that the phase velocity of x rays within most media is greater than the speed of light and incident rays from a vacuum refract away from normal incidence.

This may be extended to allow for anomalous dispersion in an ad hoc way using

$$\frac{F_0}{V} \simeq n_e = \frac{N_A \rho}{M_w}\left[Z_m + \sum_i Z_i\left(\frac{\lambda}{\lambda_i}\right)^2 \ln\left|1-\left(\frac{\lambda_i}{\lambda}\right)^2\right|\right],$$ (4)

where i is summed over all orbitals and Z_i refers to the number of electrons in orbital i. This correctly predicts the approximate overall shape of each edge (neglecting the fine structure), but with a dip at the edge reaching the unphysical value of $-\infty$. The latter occurrence may be corrected by the addition of small semiempirical terms to the argument for the log term, but then the equation is no longer well defined or readily calculable from standard tables. Several such equations are derived in Ref. 13, where the agreement of form is good, but errors of one or more electrons (in F_0) arise for iron and calcium below or near the edges. In such regions of anomalous dispersion near the absorption edges, the value of the overall structure factor can fall below zero, in which case refraction has the same sign as for conventional visible optics. A consequence of the phase velocity of x rays that are slower than the speed of light is the possibility of Cerenkov radiation produced by relativistic electrons. This has been observed in the soft x-ray regime.

For first-order radiation in the angular (Bragg) range of 0.65–1.15 rad for typical crystals, centroid shifts are dominated by the refractive index correction, [from Eq. (1)]

$$\frac{\Delta\lambda}{\lambda} = \frac{\lambda_C - \lambda}{\lambda_C} \simeq \left(\frac{2d}{n\lambda}\right)^2 \delta,$$ (5a)

where λ_C is the wavelength inside the crystal. This corresponds to a shift of the peak angle from the Bragg angle by

$$\Delta\theta = \theta_C - \theta_B = \arcsin\sqrt{\delta(2-\delta)+\left(\frac{n\lambda}{2d}\right)^2} - \arcsin\left(\frac{n\lambda}{2d}\right)$$

$$\simeq \delta\left(\frac{2d}{n\lambda}\right)^2 \tan \theta_B.$$ (5b)

Note that $\delta \propto \lambda^2$, so that the shift is approximately proportional to $\tan \theta_B$. For a flat crystal geometry and a flat detector (normal to the principal ray) at distance R, this yields a shift across the detector of

$$\Delta Y = R \tan(\theta_C - \theta_B) \simeq R \Delta \theta. \tag{5c}$$

A positional sensitive detector such as a proportional counter will be able to measure this shift. In the Johann curved crystal geometry, detection is made on the Rowland circle after focusing, so that an arc around the Rowland circle ΔY_z relative to the Bragg location may be defined. A flat detector is commonly used with curved crystal geometries for simplicity or mechanical reasons rather than the ideal narrow curved detector on the Rowland circle. For locations off the pole axis (where the Rowland circle and diffracting crystal coincide), evaluation of this becomes complicated.[17] To first order, $Y_z = 2R_z \theta_{out}$ where R_z is the Rowland circle radius, and $\theta_{out} = \theta + \alpha_p$ is shifted in asymmetric diffraction by the angle of the diffracting planes to the surface α_p, so

$$\Delta Y_z = 2R_z \Delta \theta. \tag{5d}$$

Within the same approximation, a detector crossing the Rowland circle at the predicted location and normal to the expected incident ray will follow

$$\Delta x = 2R_z \sin \theta \, \Delta \theta. \tag{5e}$$

These refractive index shifts scale as n^{-2}, diminishing rapidly with order.

C. Comparison of semiempirical forms

Figure 1 compares the approximations represented by Eqs. (2)–(4) when implemented in Eq. (5b) in exact or approximate form. These may be compared to implementation of Eq. (6), representing the standard route of dynamical diffraction theory. Neither the use of Eq. (5b) nor the use of Eq. (6) is exact, since both neglect contributions of the order of δ^2. Indeed, the definition of the "refractive index correction" is itself uncertain. Within this paper, the definition to be adopted is given in Sec. II D, as represented heuristically and in approximate form in the preceding text, while a more careful critique shall be reserved for a subsequent discussion. (On this issue, see also Ref. 14.)

A comparison of the estimates from these equations is enhanced by crystal data. In this paper, we give examples for germanium, silicon, PET [pentaerythritol, $C(CH_2CHOH)_4$], and ADP (ammonium dihydrogen phosphate, $NH_4H_2PO_4$) crystals diffracting in various orders of the 422, 111, 002, and 101 planes, respectively. These represent a useful range of crystal perfection and character in the 0.1–11 Å interval, with $2d$ spacings in first order being 2.3098, 6.27121, 8.7358, and 10.641 Å, respectively. Crystal and form factor data are discussed in Refs. 18 and 19, and primarily follow Refs. 15 and 16 as well as Refs. 20–24.

Equations 3 and 4 are generally inadequate by 3%–12% or more near any edge structure of individual atomic form factors, or up to 1%–2% far away from the edges [Fig. 1(a)]. Conversely, the use of Eqs. (2) and Eq. (5b) in exact or approximate form is usually in agreement with standard dynamical diffraction at the 0.1%–0.2% level over most of the angular range. For Si 111 at high Bragg angles, errors of the simpler estimates easily reach 6% or 15%, where even im-
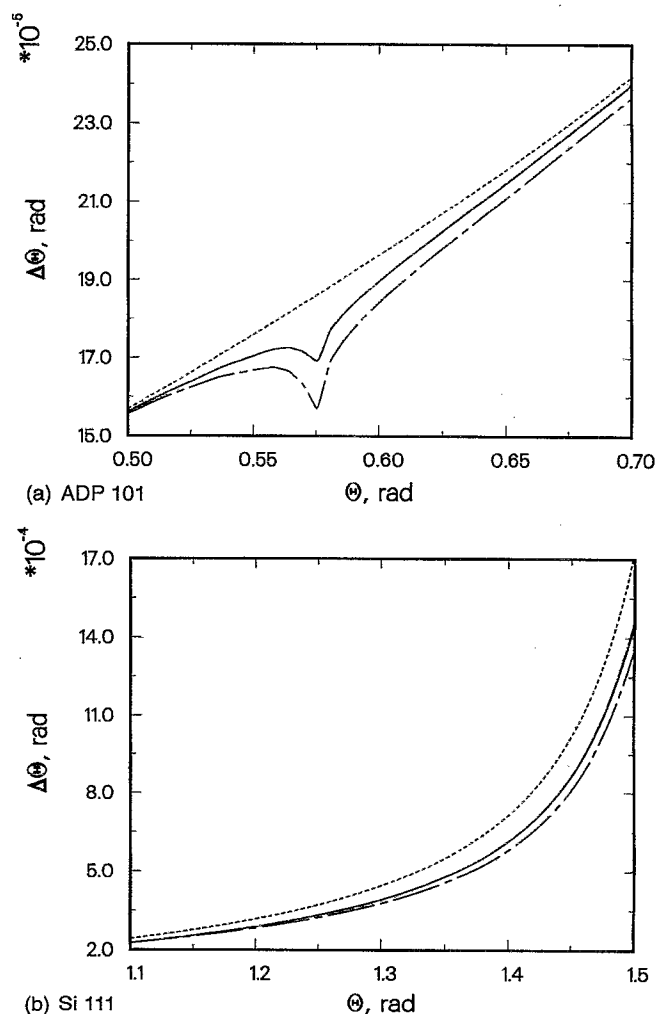

FIG. 1. (a) Estimates of *refractive index corrections* to the Bragg angle for ADP 101 planes in the region of the P K edge: Eq. (3) (dash) and (4)(--) deviate by up to 12% from accurate formulas or experiment near the edge and 1%–2% at a distance of 7° away, while Eq. (5b) (·) and (6) (—) appear coincident on this scale. (b) Estimates of refractive index corrections to the Bragg angle for silicon 111 planes above 63°. At near-normal angles, Eqs. (3) (dash) and (4) (--) err by 19% and 7% while Eqs. (5b) (·) and (6)(—) differ by 1%–2%.

proved estimates can differ by 1%. The larger errors remain at several percent for Bragg angles above 66° and 49°, respectively.

Three conclusions can follow from these observations: (1) Equations (2) and (5b), or Eq. (6), should be preferred to alternate forms. (2) Regions of near-normal incidence or of absorption edge structure should be avoided when possible in the pursuit of precision wavelength measurements. (3) Detailed profile calculations can avoid or minimize this uncertainty in refractive index corrections.

D. Modification for asymmetric diffraction

A deviation parameter y is commonly defined to include the effects of polarization and crystal asymmetry using

$$y = \frac{\frac{1-b}{2}\,\psi_0' + \frac{b}{2}\,\alpha}{\sqrt{|b|}\,|C\psi_H'|}, \qquad (6)$$

where $\alpha = 4(\sin\theta_B - \sin\theta)\sin\theta_B$, ψ_H' is the real part of the Fourier component of index H of 4π times the polarizability, given by $\psi_H = -(r_0\lambda^2/\pi V)F_H$; C is the polarization factor [$=1$ for the normal component (π polarization), or $|\cos 2\theta|$ for σ polarization], and b is the ratio of direction cosines (γ_0, γ_H) of the incident and diffracted (reflected) beams relative to the normal to the crystal (lamellar) surface. Note that there are two converse conventions for polarization states, both widely used; herein the unattenuated polarization with the electric vector perpendicular to the scattering plane is defined as π polarization and therefore has a polarization factor $C=1$. Commonly, this is the same as the electric vector being parallel to the surface. The other convention would normally reverse the labeling of the polarizations. For symmetric Bragg diffraction, $b=-1$ (but see Ref. 25 for qualifications in the use of these parameters in the tails of Bragg peaks or at grazing incidence diffraction). The refractive index shift from the Bragg angle (corresponding to $y=0$ at the profile center) then reduces to Eq. (1). In symmetric Laue diffraction $b=1$ and this correction disappears. More generally, this results in a refractive index correction given by Eqs. (1), (5a) and (5b) but with δ and hence $\Delta\theta$ scaled by $(1-1/b)/2$.

This relates to the shift of *incident* angle of the profile; for the output angular shift, direction cosines are interchanged so $b \rightarrow 1/b$. Here, the dominant shift of the peak angle arises from the mean angle (α_p) of the diffracting planes at the surface to the surface normal—zero for the symmetric case. Assuming that $\theta_i = \theta_r$ (the angles of incidence and reflection with respect to the diffracting planes are equal), which is accurate below the level of other simplifications, this is related to b using

$$b \simeq -\frac{\sin\theta_{\text{inc}}}{\sin\theta_{\text{out}}} = -\frac{1}{\cos 2\alpha_p + \sin 2\alpha_p \cot\theta_{\text{inc}}}, \qquad (7)$$

where θ_{inc} and θ_{out} are the incident and outgoing grazing angles relative to the crystal surface. For a finite, divergent source or for curved crystals, this prescription is complicated by the variation of b with surface location and with penetration depth, respectively.

Experiments using collimated parallel incident beams may measure deviations of diffracted wave exit angle relative to the crystal or relative to the incident beam; in the latter case the deviations of α_p would cancel. In the former case, or where broad sources emitting in 4π are used, the full shift of α_p in angle of emission may be observed. The refractive index contribution to this shift, relative to the incident beam, is given by the sum of the inward and outward deviations, by Eq. (5b) scaled by $1-(b+1/b)/2>2$. In the symmetric Bragg case this factor is exactly 2.

Shifts of the exit angle relative to the crystal surface, as may be measured on detectors observing broad sources where the incident angle may be ill-defined, would involve a scaling of $(1-b)/2$ from the above. An example is given in Figs. 2 and 3 for $\alpha_p = 17.5$ mrad (1°) and the diffraction from
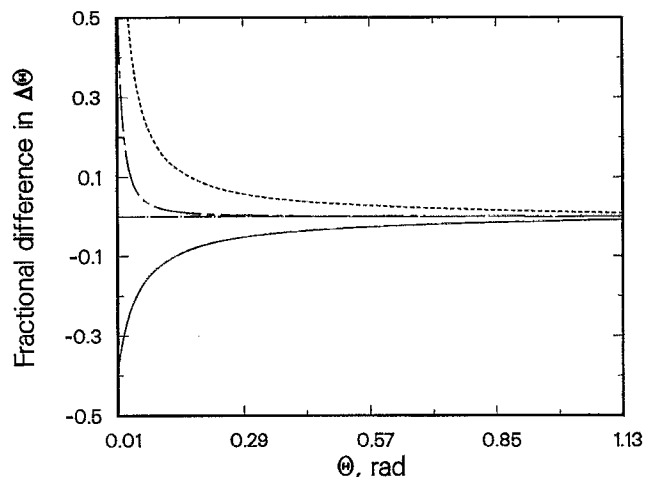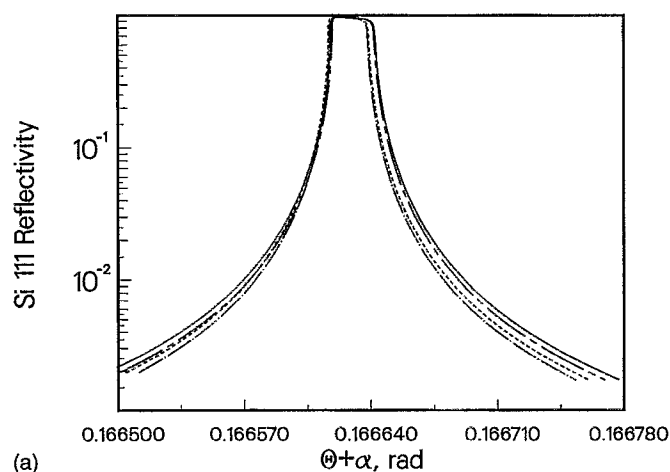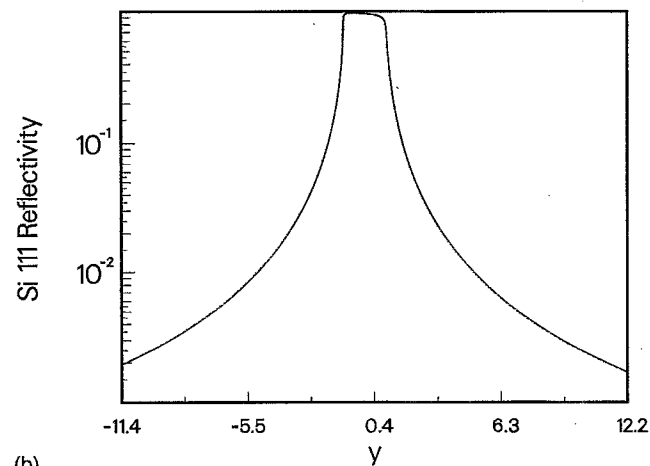

FIG. 2. Plot of the effect of *asymmetric diffraction*, $\alpha_p = 17.5$ mrad, on the refractive index correction from the $y=0$ location to the Bragg angle. The solid curve indicates the fractional difference in the shift of the *exit* angle for asymmetric vs symmetric (Bragg) diffraction. The dashed curve repeats this for the incident angle, while the third curve relates to the difference between incident and exit angles.

FIG. 3. (a) The effect of asymmetric diffraction on Si 111 rocking curves for π (full line) and $\sigma(--)$ polarizations. Asymmetry with a misalignment of $\alpha_p = 17.5$ mrad is indicated by dashed and dot-dashed lines, respectively, on the angular scale $\theta + \alpha_p$. (b) The same comparison as in (a), but on the y (diffraction coordinate) scale.
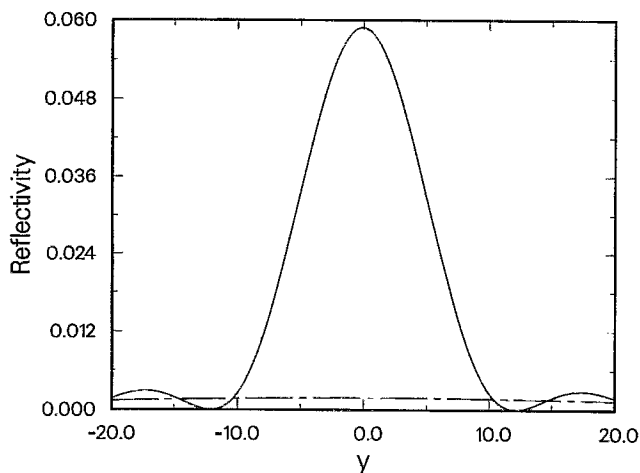
FIG. 4. Diffraction profile for a thin (0.4 μm) Si 111 crystal, at 0.7 rad. Reflected (diffracted) ratios are indicated for π polarization and the weaker σ diffraction. Note that the convention used for choice of polarizations is discussed in Sec. II D; herein the unattenuated polarization with the electric vector perpendicular to the scattering plane is defined as π polarization.

Si 111 crystals. The effect of asymmetric diffraction on the refractive index shift is 7% of the total correction when the incident angle is reduced to 12°, but is still 2% at 45°. The effect on the exit angle relative to the incident angle is much less pronounced, being only 0.6% of the total refractive index contribution at 12°. Note that reductions of the angular shift by 12% correspond to reductions of the angular diffraction widths by the same fraction, but that profiles and widths on the diffraction coordinate scale y are invariant.

A simple solution is to measure the angle of the diffracting planes to the surface to high accuracy or to transform profiles to a $\sin \theta$ scale before further analysis is conducted. Often these alternatives are not available or convenient, but this uncertainty or shift can be minimized by the use of higher Bragg angles.

E. Peak profile asymmetry

Estimates of shifts based on Eq. (6) or on a scaled version of Eq. (5) following Sec. II D neglect profile asymme-
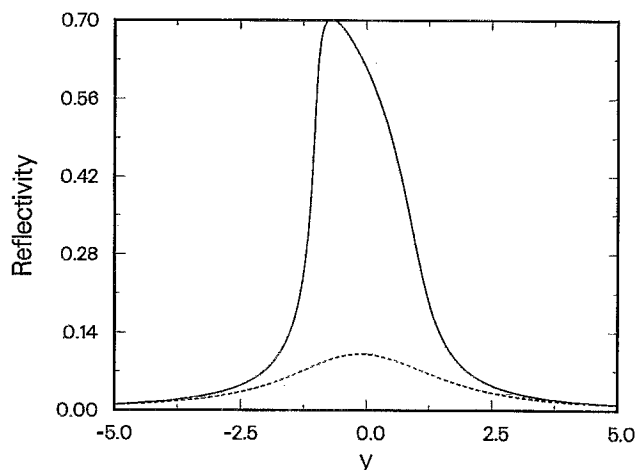

FIG. 5. Diffraction profile for a thick (1 mm) Si 111 crystal, at 0.7 rad. Bragg reflected (diffracted) ratios are indicated for π polarization and the weaker σ diffraction. The π polarization has a clear asymmetry relative to the $y=0$ location, with a peak near $y=-1$.

try. The corresponding peak shift is dy with $-1 \leqslant dy \leqslant 0$, where $-1 \leqslant y \leqslant 1$ covers the ideal diffraction (Darwin) width. A nonabsorbing perfect crystal has $dy=0$ and a top-hat profile. Very thin crystals also have $dy \rightarrow 0$ with wide Pendellösung oscillations (Fig. 4). However, most real (thick) crystals in first-order diffraction have a peak for π polarized radiation at $dy \rightarrow -1$ (Fig. 5). This is a direct consequence of the preferential absorption with increasing dy, or equivalently a consequence of the imaginary component of the structure or form factors of the crystal. This corresponds to a shift reducing the refractive index correction by up to 50% or more (though usually smaller). For the incident wave and angle, this is

$$\sin \theta_P - \sin \theta_C = \frac{\sqrt{|b|} |C \psi'_H| dy}{-2b \sin \theta_B},$$

$$dy = \begin{cases} \rightarrow -1, & \pi \text{ polarization or } \sigma, \text{ away from } \pi/4 \\ \rightarrow 0, & \sigma \text{ polarization near } \pi/4 \end{cases} \quad (8)$$

For the angular shift of the outgoing wave relative to the diffracting plane, this may be approximated by

$$\Delta \theta(P-C) \simeq \left(\frac{b}{\sqrt{|b|}} \right) |\psi'_H| dy \left(\frac{|C|}{2 \sin \theta_B \cos \theta_C} \right), \quad (9)$$

where the first bracketed term is unity in symmetric Bragg diffraction and the last bracketed term contains the explicit angular (energy) dependence of the shift. σ polarized radiation is near symmetric, with dy and any consequent effect vanishing, at angles near $\pi/4$ rad.

For dy constant, $|\psi'_H| \propto \lambda^2$ gives a dependence upon the Bragg angle similar to Eq. (6) (Fig. 6) (but dy is not generally constant with the angle). This contribution is maximized for first-order radiation and decreases rapidly with increasing diffraction order. This estimate may typically exceed the real (mean) shift by a factor of 4 or more, reflecting the smooth and gradual decline of reflectivity from the indicated peak to the $y=+1$ location [as opposed to a δ function at $y=-1$ as suggested by the first part of Eq. (8)]. For sufficiently thin or nonabsorbing crystals, the actual shift from this source may be very close to zero (as often for σ polarization and as opposed to the above estimate). There is a regime of intermediate crystal thickness where flat crystal centroid locations depend on this thickness, but the precision of results is generally not limited by the corresponding uncertainty (cf. Table I).

This discussion has remained general regarding the actual spectrometer geometry involved, although results have been given explicitly for a single-crystal device. Considering only flat crystal diffraction, there are numerous parallel, antiparallel, or other multiple crystal spectrometer arrangements for monolithic crystals or separate elements. The reader is referred to Ref. 26 or other sources for a detailed discussion of these geometric and spectroscopic arrangements. Scans and measurements may be provided by varying the final crystal diffracting angle with respect to the axis of the first; or by rotating the angle around the normal to the diffracting planes (for asymmetric diffraction or multiple-beam studies); or by varying angles symmetrically or asym-
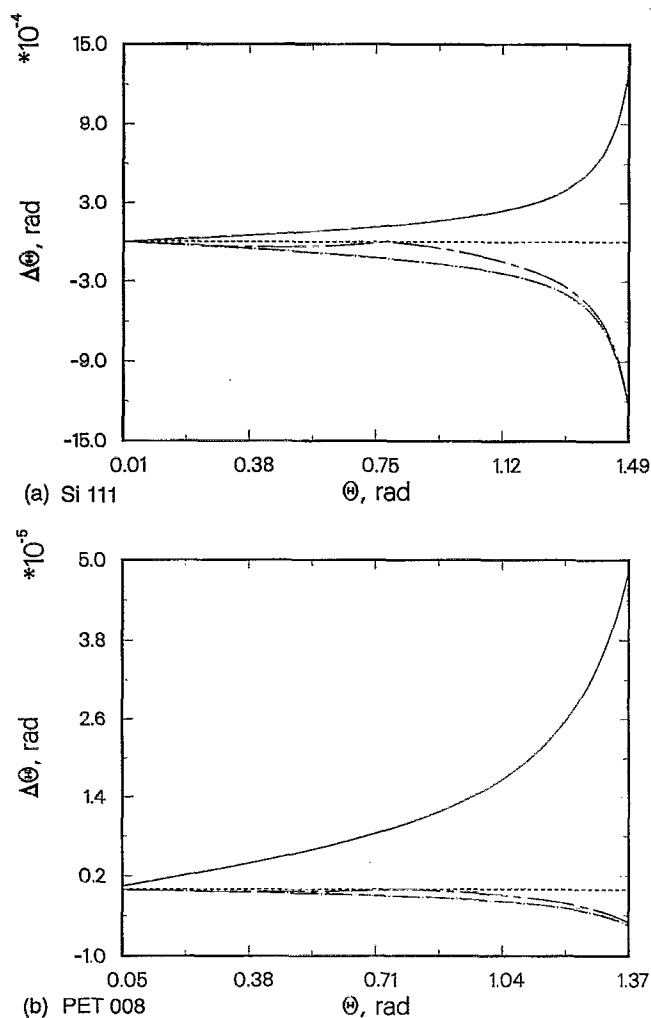
FIG. 6. *Profile asymmetry* given by the $y=0$ to $y=-1$ shift for π and σ polarizations $(--;\cdot-)$ compared to refractive index shift following Eq. (6) (full line). (a) For silicon 111 in first order, both polarizations show asymmetry of the same magnitude as the refractive index estimate for much of the angular range. (b) For PET 008, both polarizations show near-symmetric profiles, with the asymmetry below the 10% level.

metrically for a double-crystal pair or for the whole system.[12,13,26–28] Where multiple separate elements are involved, the number of independent axes and free parameters allow greater flexibility in the scanning procedures while also increasing the difficulty of the alignment process itself. For example, in a parallel double-flat crystal geometry (often denoted $+,-$) with identical crystals in both positions, where the angular acceptance is large compared to the diffraction width, the peak occurs in the true parallel position, while the zero location could be aligned with the mean diffracting angle (e.g., with a broad detector) or with the peak diffracting angle (with a narrow detector) broadened only by the natural linewidth and the source size. The overall shift due to profile asymmetry will generally be a convolution or superposition of single-crystal elements, which individually follow the relations given above. Additionally, the extreme limits represented by $dy=-1$ and $dy=0$ are not exceeded.

Some devices make use of asymmetric cuts relative to the diffraction planes, in order to suppress higher-order radiation or change outgoing divergence.[29,30] Others vary the

crystal types used in the different x-ray optical elements, to improve the resolution or control the bandpass.[31] Again, the detector may be represented by a rectangular slit or by a more complex position-sensitive device. This kind of complexity is not of direct concern in the current paper. Single-crystal results should be convolved together following the appropriate geometry.[12,13]

If only the final crystal element is rotated, relative to the optimized peak orientation, then the $(+,-)$ geometry mentioned above (with a broad detector) has a peak broadened by the first crystal profile and shifted toward the mean value, with a resulting symmetric profile. Conversely, the rotation of a narrow or position-sensitive detector in the precisely parallel arrangement yields an asymmetric, narrowed profile of higher resolution than the single-crystal result, which is shifted toward the peak value. In general, the observed peak and mean values are dependent upon the spectrometer geometry and alignment, but lie between the single-crystal peak and mean values.

Although the contributions in Secs. II A–II D are reasonably well defined, the effect in this section is difficult to evaluate separately from a dynamical diffraction calculation. Instead, we have indicated upper and lower limits for the effect, which are typically uncertain at a few percent of the refractive index correction. Some procedures model reflectivity profiles (following conventional two-beam dynamical diffraction for flat crystals) as a function of angle and then derive the mean shift from the Bragg angle. This explicitly avoids the approximations represented by Eqs. (3)–(5), and is equivalent to the use of Eq. (6). More important, this procedure represents a considerable improvement over the foregoing asymmetry estimates, as the centroids can be evaluated explicitly for the appropriate crystal thickness (and even spectrometer geometry). The problem of evaluating systematic shifts is then partially reduced to a computational problem.

F. Databases, crystal structure, and purity

The sources for crystal data illustrated in Sec. II B have their own uncertainties which can dominate in the calculations for some crystals and angles. This also assumes that impurities or variations between crystals of the same type can be controlled or minimized.

Silicon is a good example, providing well-defined crystal data with high lattice perfection and good form factor data in the energy range considered. For example, the form factors should be accurate to better than 1% in Fig. 1(b). In many angular ranges this small form factor uncertainty can provide the limiting accuracy of refractive index corrections and of dynamical diffraction calculations of the profile asymmetry.

Other crystals and energies have relatively large form factor uncertainties or relatively large atomic position uncertainties, particularly those crystals which are not monatomic. Uncertainty in the form factors (typically at the level of a few percent for low to medium energies) commonly dominates over coordinate imprecision in the determination of the structure factor F_H for Eq. (2) or Eq. (6), and hence for determining profile shifts. In particular regions, form factor

uncertainty can dominate over other systematic contributions, including refractive index corrections.[32,33]

G. Multiple beam interaction: Forbidden reflections

Major effects on asymmetry, reflectivity, and systematic shifts occur near "forbidden" reflections or where interference occurs with additional diffracting beams. These locations depend on the orientation of the crystal in aligning the additional reciprocal lattice points to near the Ewald sphere.

This occurs, for example, in the 442 reflection of silicon. Figure 7 indicates the locations of resonance with additional beams in diffraction from the silicon 442, 111, and 444, ADP 101, and Ge 422 planes. A lower wavelength limit has been introduced since the number of curves (interactions) roughly follows the inverse cube of λ.

Kinematically, in the weak field limit, each interaction contains an infinity, so that the peak reflectivity (in the original direction) will either be zero or will be increased by
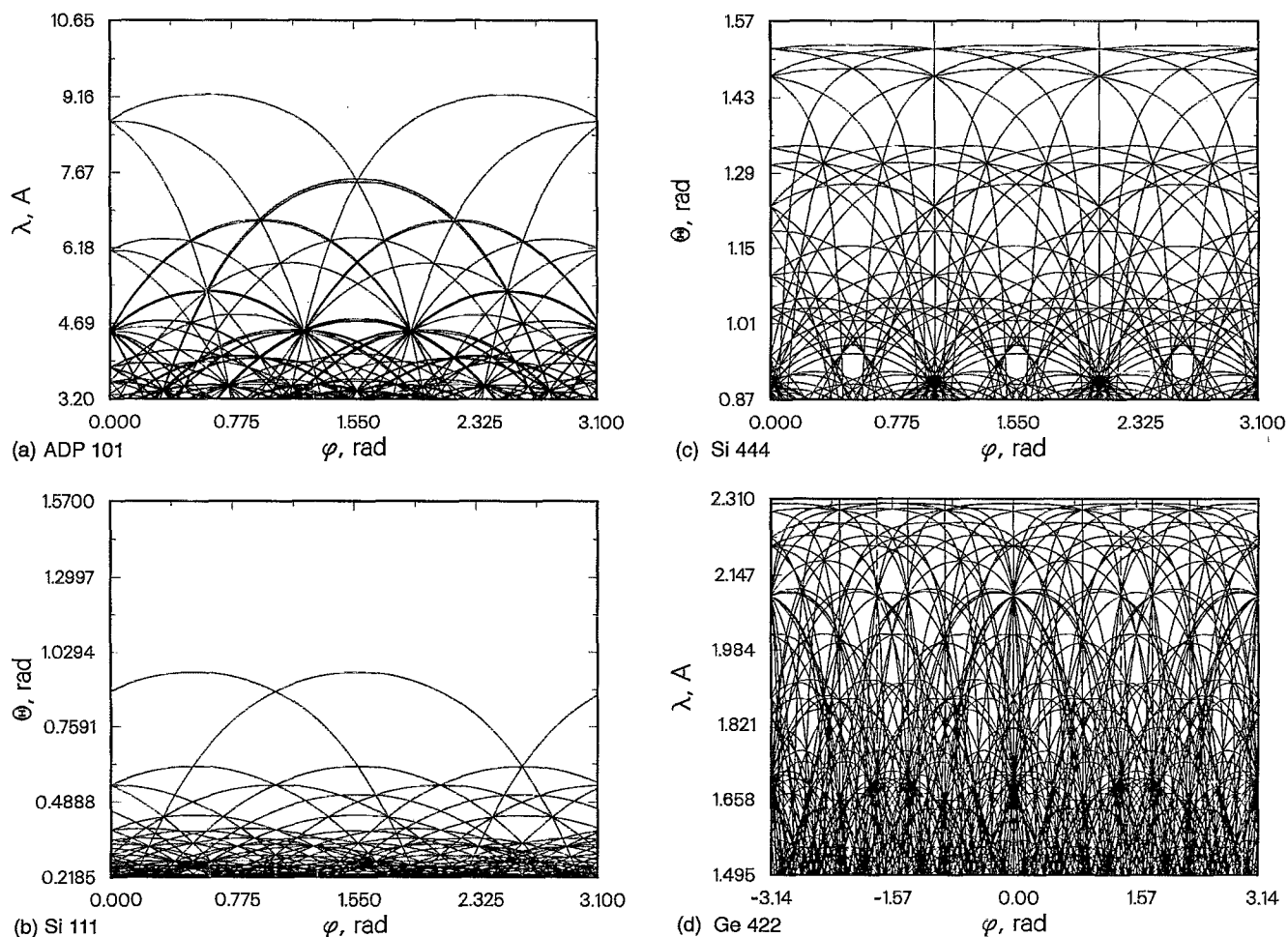

FIG. 7. Plot of *resonances* in the (two-beam) diffraction profiles due to interaction with a third (diffracted) beam. Plots of wavelength (λ, Å) or Bragg angle (θ, rad) vs the azimuthal angle (ϕ, rad). ϕ is measured relative to the normal to the lowest hkl Bragg plane providing an interaction in the plot region. ϕ covers 2π rad, but the plots are symmetric. In the plots, each curve represents the peak interaction of one or more (off-axis) lattice planes with the primary and normal diffracted waves. (a) Three-beam resonances in ADP crystals with the normal diffracted beam reflected from the 101 planes, relative to the 001 normal. These planes provide vertical lines on the plot at $\phi=0$, π. The highest two λ curves on the plot are due to interactions from 011, 0–11, 1–10, and 110 planes, respectively; the doublets (beginning at 7.55 Å) arise from 002, 10–1 vs 200, −101 planes (due to the inequality of the a and c lattice vectors). At $\theta=17.5°$ or $\lambda=3.2$ Å, there are 1048 interactions in 2π, or 262 "interfering" planes, commonly overlapping to provide ~262 curves in 2π. (b) Three-beam resonances in Si crystals with the normal diffracted beam reflected from the 111 planes, relative to the 004 normal. These planes provide curved lines on the plot beginning at $\lambda=2.65$ Å. The highest λ curves on the plot are due to interactions from 1–11 and 11–1 planes, respectively. At $\theta=12.5°$ or $\lambda=1.36$ Å, there are 960 interactions in 2π, or 240 interfering planes, providing ~480 curves in 2π. (c) Three-beam resonances in Si crystals with the normal diffracted beam reflected from the 004 normal. These planes provide vertical lines on the plot at $\phi=0$, π, with 400 and 040 planes providing vertical lines at $\phi=\pi/3$ and $2\pi/3$, respectively. The curves for the hkl planes superimpose with those for $444-hkl$. The highest 3 λ curves on the plot are due to interactions from 18 odd-index planes. At $\theta=50°$ or $\lambda=1.20$ Å, there are 960 interactions in 2π, or 240 "interfering" planes, providing circa 240 curves in 2π. (d) Three-beam resonances in Ge crystals with the normal diffracted beam reflected from the 422 planes, relative to the 00–2 normal. These planes provide curved lines on the plot beginning at $\lambda=1.718$ Å, with 002, 022, 020, 400, 402, and 420 planes providing vertical lines. At $\theta=40.2°$ or $\lambda=1.4938$ Å, there are 792 interactions in 2π, or 198 interfering planes. (e) Three-beam resonances in Si crystals with the normal diffracted beam reflected from the 442 (forbidden) planes, relative to the 004 normal. These planes provide curved lines on the plot beginning at $\lambda=1.706$ Å, with 224 and 400, 040 planes providing vertical lines at $\phi=0$, π and $\phi=-1.25$, 1.89, respectively. Note that these planes are allowed, but that the three-beam interaction is proportional to $F(hkl)F(hkl$-442), the latter of which is forbidden. A consequence is that vertical lines shall occur with equal intensity at $\phi=-1.89$, 1.25 due to the forbidden planes 402, 042. At $\theta=48.7°$ or $\lambda=1.36$ Å, there are 624 interactions in 2π, or 156 interfering planes.
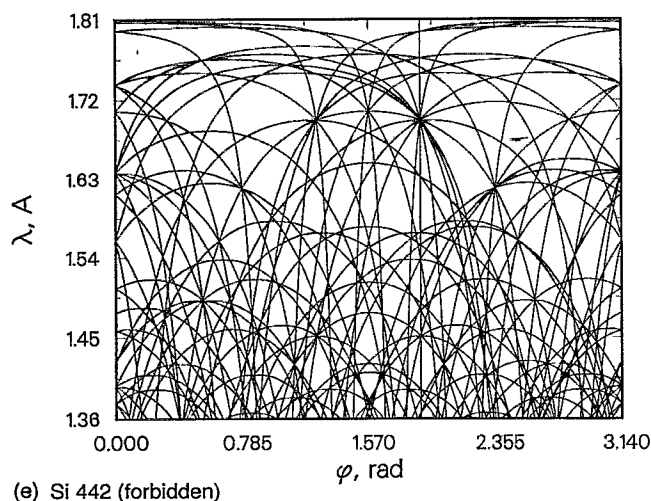
(e) Si 442 (forbidden)

FIG. 7 (*Continued.*)

many orders of magnitude (subject to energy conservation). Despite the simplicity of kinematic models, this dramatic suppression or amplification has been observed.[34–36] With this strength of interaction, the critical issue here relates to the widths of these features in azimuthal angle ϕ (the angle in the primary diffracting plane, normal to the plane of incidence and relative to some secondary plane).

The kinematic approximation becomes increasingly valid as ϕ is shifted away from the interaction resonant location. One estimate of the interaction width in ϕ space is then given to a reasonable approximation by the distance from the resonant center at which the effect of the third beam gives a doubling of the intensity (in the kinematic model).

For a weak or forbidden primary diffracted beam, the dominant effect of most secondary diffracting beams will be to enhance the profile by orders of magnitude. The "interaction width" mentioned above is then considerably larger than the FWHM (full width at half-maximum). Lower order, stronger interfering reflections have (much) larger interaction widths. If the value of ϕ lies within the interaction width, the effect on intensities, asymmetry, and systematic shifts can be large.

Extreme cases are indicated by planes such as silicon 442 [Fig. 7(e)], where the reflection is geometrically forbidden so far as the spherically symmetric atomic form factor is concerned, but is allowed by (weak) scattering from the different site symmetry of the bonding orbitals. For this reflection, the interaction width with the $-1,1,-1$ planes at 1.543 35 Å is measured to be 1.4° or 2.1° (depending upon the phase and shape of the interaction). A simple estimate based on the result of Shen[36] yields an estimate within a factor of 2 of this, and enables some qualitative conclusions to be drawn. The *maximum* interaction widths in ϕ space occur at the lowest energy for a given interaction, which is also the region of *narrowest* width features in λ or θ profiles (and vice versa). Interactions with forbidden reflections, or with reflections whose complement is forbidden, have essentially negligible widths in either space. Maximum widths in ϕ space for interactions with strong reflections regularly reach ten degrees. The profile and hence detailed effect of

such an interaction depends on the multiplicity of interactions, their phases, and relative strengths, but may at least be estimated in the single interaction (i.e., three-beam) assumption.

For interactions with only a single plane, the coverage of ϕ space in this case (Si 442 at 1.81 Å) exceeds 1%; as 1.54 Å, or 58° Bragg angle is reached, this has increased to about 26° coverage or 7%–8%. Interaction regions increasingly overlap one another and the probability of significant interaction for a given wavelength and azimuthal angle becomes large. The two-beam diffraction profile width of 10^{-3}–10^{-5} degrees is easily dominated by the 0.004°–0.29°–1.33° interaction widths in θ_B space. Hence in passing through the diffraction profile, each side of the peak will be amplified (or suppressed) by large and asymmetric factors. Around the peak, this will typically shift the centroid shift due to profile asymmetry from $y=-1$ to $y=+1$ (outside this region the rate of decline of the reflectivity will often exceed the rate of increase of the three-beam induced asymmetry). This can then be as large as or larger than the peak profile asymmetry discussed earlier, and hence as large as the refractive index corrections.

H. Multiple beam interaction: Allowed low-order reflections

ADP 101 and silicon 111 [Figs. 7(a) and 7(b)] represent near-ideal cases where the lowest order strongly diffracting plane is considered. Here for high Bragg angles there is no competing third diffracting plane, and this effect cannot occur. Even at medium angles (e.g., 45°) there are only a few interactions, but as the Bragg angle is reduced below 20° these planes and interactions proliferate. Above 10°, orientation of the azimuthal plane of the crystal by rotation of ϕ, to higher and higher precision with decreasing wavelength, can explicitly avoid such interactions. At sufficiently low angles, this procedure will again exceed the precision of the source and crystal alignment, even if the orientation is known to high precision. Near grazing angles, or in the low-angle tails of Bragg peaks, the Fresnel (or 000) beam and reflection becomes dominant and must be included (separately from any other multiple beam interactions).[25]

These allowed and low order planes (ADP 101, Si 111) have much fewer and weaker interactions than presented in Sec. II G, with maximum widths in ϕ space of the order of 0.001°–0.0001° leading to quite small percentage coverages. Diffraction widths of the order of 0.01°–0.001° also dominate over typical interaction widths of 0.0006°–0.000 001° (except for the curves of constant ϕ), so that three-beam interactions appear as rapid fluctuations on top of a narrow region of the normal two-beam profile. Here induced asymmetric shifts of centroids would generally be considerably smaller than the peak profile asymmetries discussed above.

I. Multiple beam interaction: Allowed medium-order reflections

For intermediate cases such as silicon 444 or germanium 422 [Figs. 7(c) and (7d)], there are interactions at all the diffracting angles. Thus, the azimuthal angle can never be

ignored, and the situation for high Bragg angles corresponds to that for low Bragg angles in the near-ideal cases (Sec. II H). Here, several hundred (or thousand) interactions occur for any given wavelength below angles of 40° or so—each interaction with a given plane in general occurring at a set of four specific azimuthal regions (following the plane and crystal symmetry). These four regions in 2π correspond to two independent curves, with an apex at the highest wavelength (or Bragg angle) for which the two planes involved interfere. Some of these interactions and some of these curves cross or overlap one another, depending upon the lattice symmetries. However, there still remain several hundred or thousand curves and interactions to be accounted for, and the alignment and tolerance on the spectrometer is typically inadequate to explicitly avoid these interactions.

For the allowed but medium-order crystal planes (Si 444, Ge 422), interaction widths in ϕ and θ are several orders of magnitude smaller than for forbidden reflections. Maximum widths for strong reflections in ϕ space range from 0.1° to 0.01°, while coverages in ϕ space at θ=0.8717 rad for Si 444, and at θ=0.7033 rad for Ge 422, are estimated at 0.18° and 0.24°, respectively. Coverages less than 0.1% imply that interactions may be avoided or neglected in many cases at these medium angles. For 1.2 Å, however, diffraction widths of 0.001°–0.000 01° approach interaction widths in θ_B space of 0.001°–0.000 001°. Then changes of intensity at far tails are negligible, but major and rapid changes occur within these widths, and hence within the profile widths, leading to asymmetries which could easily correspond to shifts of the mean diffraction coordinate by δy = ±2 or more.

In the high-angle cases, measurement of crystal orientation can allow these interaction regions to be avoided, but this is not true for the higher order diffraction and lower wavelength regions. Also, the use of calibration lines or other relative measurement techniques cannot address this source of error or systematic correction unless a dense set is available. In all cases, however, high experimental resolution should confirm or eliminate hypothesized effects of three-beam interactions. Diffracted intensities much larger or smaller than expected provide an indication for these interactions. The rapid oscillation of intensities over (narrow) ranges of the smooth diffraction profile, separate from and superimposed upon the Pendellösung, is also a strong indicator of these interactions. The symmetry of these features is often able to determine ϕ to better precision than may be possible from alignment considerations. Two-dimensional detection is able to identify changes of (convolved) reflectivity with the variation of λ and ϕ, and hence provide much more restrictive limits on possible multiple beam interactions.

J. Tertiary corrections

For flat crystals, this essentially completes the summary of effects leading to systematic shifts of the Bragg angle or detector position for centroids around diffraction peaks. Figure 8 illustrates the agreement of the sum of these estimates with detailed profile calculations.
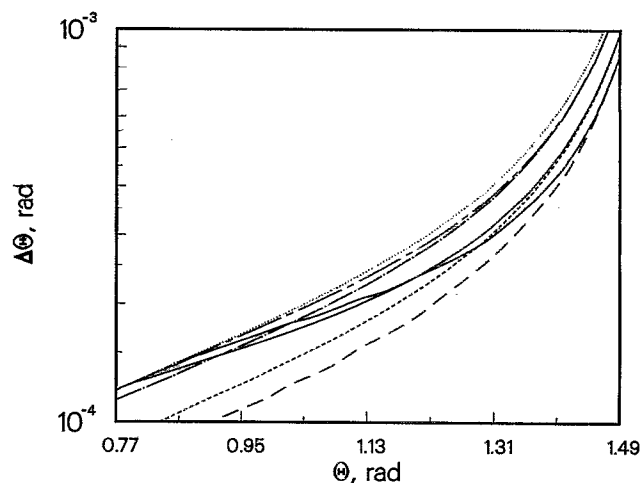

FIG. 8. Sums of contributions to flat crystal peak or centroid values for Si 111 diffraction. The refractive index shift, Eq. (6), is given by ··· while the estimated mean based on a peak at $y=-1$ is indicated for σ and π polarization by the solid and long dashed lines converging at normal incidence; the actual peak for T=0.4 mm is indicated by solid and short dashed curves, converging at normal incidence. The latter corresponds approximately with $y=-0.33$, and there is fairly good agreement of the final mean shift (–– and ·–, respectively) with a value corresponding to $y_{peak}/4$.

Corrections to the above prescription include the accurate derivation of a mean dy value from estimates of asymmetry and the use of a more exact arcsin expression [from Eq. (6)] rather than the simplified form indicated in Eq. (5b).

Mosaicity has potentially significant effects on centroid location, defocusing or broadening asymmetric profiles to center more on θ_C than θ_P. This is important for thick crystals (as defined by Sec. II E) when the mosaic block size lies in the thin or intermediate regime. The profile asymmetry and mean can then be sensitive to the mosaic parameter and be shifted toward θ_C by the amount discussed in Sec. II E.

The overall asymmetry can significantly affect centroid determination of experimental profiles, depending on the fitting function. Additional broadening from Doppler effects in the source or natural linewidths will convolve the asymmetry and lead to uncertainty in centroid determination. Asymmetries of tails become important at the 5%–10% level and are the subject of a succeeding paper.

General flat crystal geometries involve broad detectors with negligible positional sensitivity, with the idealized location collecting (integrating) most radiation diffracted from a given plane (or planes). However, the possible use of a narrow or position-sensitive detector will then involve concern for the profile shape and location at a given distance; and hence involve correction or allowance for lateral shifts upon depth penetration. This is usually of negligible significance for flat crystal measurements, while being of significance for curved crystals. Thus, it will be discussed in Sec. III. The thermal loading of a flat crystal, as is important for synchrotron sources and hot plasmas, leads to stress and distortion of the lattice planes and diffraction; usually this creates an effective crystal curvature and so will be addressed briefly in Sec. III.

Some of these corrections require evaluation of a (full) dynamical diffraction theory; others require careful ray tracing or convolutions of x-ray optical elements.

K. Summary of Sec. II (flat crystal systematics)

Experiments requiring absolute wavelength determination to better than 100 ppm in the x-ray regime must generally involve careful consideration of a variety of effects in addition to refractive index corrections. Although simple estimates for the latter can be accurate to a few percent, there are significant regimes where these simple estimates are inadequate at the 5%–20% level. There are relatively well-known modifications of these corrections due to the nonparallelism of diffracting planes with the surface, of similar magnitude. Uncertainties in the angle of the diffracting planes to the surface can provide significant uncertainty in experimental results, even when simple formulas are avoided and detailed computations are performed. Profile asymmetry due to dynamical diffraction can be of the same magnitude as refractive index corrections themselves, particularly for low-order diffraction of soft x-ray π-polarized radiation with thick crystals. The azimuthal angle is often quite uncertain, and can lead to large shifts of diffraction profiles due to multiple diffraction. Often this uncertainty can be eliminated by experimental design.

For flat crystal diffraction, these contributions are relatively straightforward, even if computationally complex, and associated magnitudes and angular dependencies have been discussed and presented in simple formulas. The variation of angular shifts with the Bragg angle can follow tan θ, cot θ, or θ independent relations, with particularly strong local features and alternate dependencies near edges or near three-beam diffraction points. The precision of profile shifts can be limited at 0.1%–1.0% of the refractive index corrections by form factor uncertainties, in optimum cases. The use of imprecise or inadequate formulas as represented by Eqs. (3) and (4) or by neglect of profile asymmetry will generally lead to large errors in derived wavelengths, well in excess of this level.

Measurements of unknown wavelengths relative to a nearby calibration line by extrapolation can increase the precision by an order of magnitude, in relation to refractive index corrections, profile asymmetry, asymmetric Bragg diffraction, and other effects, but requires an understanding of the functional relations indicated above for higher precision. Locally, this can be provided to first order by the slope of the response between several calibration lines. However, cancellations of the effects of most absolute shifts assume that the relative measurements are made in the same order and with nearby Bragg angles, away from absorption edges and away from extreme spectrometer angles.

Multiple-beam interactions are generally not determined or accounted for in such calibrations. If the azimuthal angle is inadequately known, other methods must be used to consider the importance of these effects. In some regimes, variation with angle of several component effects is far from constant or linear. Care should be exercised in avoiding these regimes or, again, in understanding the expected functional dependencies and relative magnitudes.

The complexity of shifts with order and polarization in spectra necessitates detailed calculations of the sort indicated here for a precision approaching 1% of the refractive index corrections. Calculated shifts agree well with the sum of simpler estimates, reproducing the dependence on the Bragg angle.

III. CURVED CRYSTAL SYSTEMATIC CORRECTIONS

A. Overview

Curved crystal diffraction displays all the effects discussed in Sec. II, but with a modulated amplitude and relative importance. Section III B considers the typical effect of curvature on the flat crystal relations. It also summarizes variable definitions, as the formulas presented are numerous and relate to effects which are not generally well appreciated.

The remaining sections address additional systematics affecting the results of curved crystal Bragg diffraction. Explicit functional forms are provided for the Johann case, although many relations are of general application. This paper is concerned with focusing and shifts dependent on the diffraction process within the crystal.

Section III C will introduce one of the potentially dominating effects for curved crystals: namely the mean penetration depth of the incident wave field. Several approximations are presented in order to indicate the degree of detail necessary for the different experimental regions. Section III D introduces the shift of the mean angle to the diffracting planes as a function of crystal depth. Section III F will discuss the lateral shift around the crystal surface of the exit location relative to the incident location of the photon. These effects of the diffraction process rather than the geometry are rarely considered and estimates are often in error by orders of magnitude.

They are correlated with effects relating to Johann aberrations, and so cannot be treated in an isolated manner (the topic of Sec. III E).

Geometrical defocusing and shifts due to the different Rowland circle and diffracting crystal radii (in the Johann geometry) leading to variations away from the pole axis are not the primary concern of this paper. However, finite source and crystal dimensions interact with defocusing shifts and diffraction corrections. Correlated results for the Johann geometry are discussed in Secs. III G–III J, which address: general principles and earlier work; crystal length along the dispersion direction; crystal and source depths; source length along the dispersion direction; and crystal and source heights. Ray-tracing packages[37] and earlier formulas[17] are often not adequate for this purpose.

A series of usually smaller corrections and effects will be discussed in a separate section, including the exact asymmetry and extinction, detection corrections, mosaicity, diffraction plane orientation, and $2d$ spacing.

High accuracy is certainly possible with curved crystal measurements in many cases, either by explicit avoidance of problem regimes or by adequate correction for the systematics involved. Precision measurements with curved crystals are often made by comparison of unknowns to calibration lines. In this case, only the difference in refractive index and

TABLE II. Basic notation.

λ: X-ray wavelength (*in vacuo*); d: crystal lattice spacing (for index H);

$2Rz$: crystal curvature radius along the generatrix (Rz is the Rowland circle radius);

n: order of diffraction; μ_r: refractive index (near unity);

F_H: structure factor for hkl index; $r_0 = e^2/m_e c^2$: classical electron radius;

ψ'_H, ψ''_H: real and imaginary parts of the Fourier component of index H of 4π times thepolarizability $\psi_H = -(e^2\lambda^2/\pi m c^2) F_H/V$; both parts are summed over real (imaginary) contributions from each scattering center so they may be complex, except for the $H \equiv 0$ ($hkl = 000$) component parts;

$\sin\theta_B = n\lambda/2d$: sine of Bragg angle; $\alpha = 4(\sin\theta_B - \sin\theta)\sin\theta_B$;

V: unit cell volume;

α_{plane}: (mean) angle of diffracting planes to the lamellar or crystal surface (along the generatrix);

C: Polarization factor [$=1$ for normal component (π polarization), or $|\cos 2\theta|$ for σ polarization);

θ_{inc}: grazing angle of incidence on crystal surface;

θ_{out}: grazing angle of emission/reflection at crystal surface;

$Y_z \simeq 2R_z \theta_{\text{out}}$; detector arc around the Rowland circle from the pole axis of the crystal [Eq. (5d)];

$b = -\sin\theta_{\text{inc}}/\sin\theta_{\text{out}} = -[1/(\cos 2\alpha_p + \sin 2\alpha_p \cot\theta_{\text{inc}})]$: ratio of the direction cosines (γ_0, γ_H) of incident and diffracted (reflected) beams relative to the normal to the crystal (lamellar) surface [Eq. 7];

$$y = \frac{\text{Re}(z)}{\sqrt{|b|}\cdot C\psi'_H} = \frac{\dfrac{1-b}{2}\psi'_0 + \dfrac{b}{2}\alpha}{\sqrt{|b|}\cdot|C\psi'_H|}: \text{ the deviation parameter [Eq. 6]};$$

θ_C: angle corresponding to $y = 0$, defining the refractive index shift;

dy: value of y for the peak of the (flat crystal) diffraction profile;

θ_P: grazing incidence angle for the peak of the (flat crystal) diffraction profile;

T: crystal thickness; μ: linear absorption coefficient.

FIG. 9. Indication of depth penetration in curved crystal Johann geometry for Bragg diffraction, with associated variables (BP, BX, XP, XZ, θ_{out}, θ_{Ax}, T, t_0, y_0) on the generatrix.

other corrections is directly relevant, and experiments can ideally achieve sensitivity of 20–30 ppm without demanding accurate values for the main corrections, as discussed in Sec. II. Calibration lines must then be measured on an absolute footing elsewhere at a similar level of precision.[15,16]

B. Variable definitions and flat crystal systematics

Equations (1)–(9) summarized the relations between the quantities in Table II and the refractive index shift, asymmetric Bragg diffraction, profile asymmetry, and multiple-beam diffraction for perfect or mosaic crystals of variable thickness.

For flat crystals, this completed the systematic shifts of the Bragg angle or detector position for centroids around diffraction peaks. Figure 8 indicates the kind of agreement commonly obtained using the estimates and relations indicated therein, compared to detailed profile calculations.

Curved crystal geometries are generally less affected by the peak profile asymmetry because the effective thickness leading to coherent diffraction is typically much less than the crystal thickness. The calculation of the flat crystal profile asymmetry component in a curved crystal calculation must therefore use a lamellar or effective thickness dependent on the curvature and diffraction, rather than the crystal thickness. An appropriate estimation of this lamellar thickness
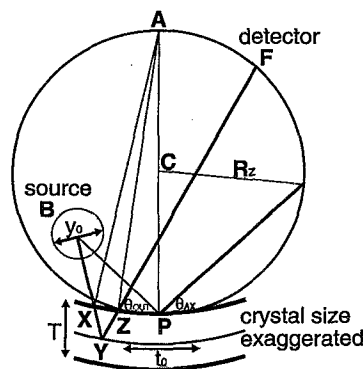
helps to ensure that coherence between contributions from nearby depths is allowed for, while the incoherence of contributions from well-separated depths is also treated. The main consequence of inadequacy in this area will be to introduce additional effective flat crystal profile asymmetry. Fully dynamical models of curved crystal diffraction, treating amplitude rather than intensity propagation, can in principle eliminate this difficulty.

The effects of multiple beam interactions are also reduced in curved crystal diffraction: both by a broadening of each diffraction width so that interactions are better represented by rapid fluctuations on the two-beam profile; and also by generally incoherent broadening from the range of crystal locations at which diffraction occurs. Hence the major shifts from Bragg angle diffraction for flat crystals (in symmetric Bragg diffraction), after curvature, are dominated in most cases by the refractive index correction. There are also many cases where the effective thickness is not significantly affected by the curvature, and where the two-beam diffraction width is not greatly increased by curvature. This depends on the crystal, thickness, curvature, and wavelength.

Flat crystal instruments tend to use broad detectors with negligible positional sensitivity, whereas positional sensitivity is usually required in curved crystal instruments in order to make use of the focusing geometry. This difference causes a shift of interest from the diffracting angle of the crystal with respect to the source, detector, or monochromator, to the location of the radiation on the detector relative to the Rowland circle and the crystal center or pole axis.[18,19] This was discussed briefly in Secs. II B and II E.

The qualitative effects discussed in flat crystals are therefore present and significant in the context of curved crystals; but the magnitudes of the corrections are often reduced, and the formulas commonly need to be reevaluated with a smaller effective crystal thickness, which may lie in the intermediate or thin crystallite regime while the crystal thickness T might correspond to the thick crystal regime (Secs. II E and II J). Other qualitative effects introduced by curvature will also tend to dominate over those corrections common to the flat crystal case.

C. Curved crystal depth penetration

Dominant contributions to higher diffraction order shifts from the Bragg angle arise from the varying mean depth of penetration with angle. To first approximation, this is due to the variation of mean grazing incidence angle at the surface compared to the Bragg angle at the diffracting planes. This effect is nonexistent for flat crystals, but can be large for even weakly curved crystals. With the linear absorption coefficient μ, crystal thickness T, and mean vertical penetration depth $\bar{d}$ (cf. Fig. 9), the resulting shift is estimated by

$$\Delta\theta_{\text{in/out}} \simeq \arccos\left[\left(1 + \frac{\bar{d}}{2R_z}\right)\cos(\theta_B \pm \alpha_p)\right] - (\theta_B \pm \alpha_p)$$

$$\simeq \frac{-\bar{d}}{2R_z}\cot(\theta_B \pm \alpha_p), \tag{10}$$

where $\bar{d}$ may be estimated using

$$\bar{d} \simeq \frac{\int_0^{T_{\max}} t e^{-\mu(P_- + P_+)} dt}{\int_0^{T_{\max}} e^{-\mu(P_- + P_+)} dt},$$

$$T_{\max} = \min\left[T, 2R_z\left(\frac{1}{\cos(\theta_B \pm \alpha_p)} - 1\right)\right],$$

$$P_\pm = (2R_z + t)\sin(\theta_B \pm \alpha_p)$$
$$- \sqrt{[(2R_z + t)\sin(\theta_B \pm \alpha_p)]^2 - 4tR_z - t^2}, \tag{11a}$$

$$\bar{d} \simeq \int_0^T t e^{-\mu t(1/\sin\theta_{\text{out}} + 1/\sin\theta_{\text{inc}})} dt \Big/ \int_0^T e^{-\mu t(1/\sin\theta_{\text{out}} + 1/\sin\theta_{\text{inc}})} dt \tag{11b}$$

$$\simeq \begin{cases} \dfrac{T}{2}, & T \ll \dfrac{\sin\theta_B}{\mu}; & (11c) \\[2ex] \left[\dfrac{1}{\mu}\right](1/\sin(\theta_B + \alpha_p) + 1/\sin(\theta_B - \alpha_p))^{-1} \simeq \dfrac{1}{2\mu_1}(\sin\theta_B)^{-1.9}, & T \gg \dfrac{\sin\theta_B}{\mu}. & (11d) \end{cases}$$

For thin crystals or high order radiation the former case [Eq. (11c), $\bar{d} \simeq T/2$] is appropriate. For thick crystals, low energies, and large Bragg angles, Eq. 11(d) yields a useful overestimate. For near grazing incidence, Eq. (11a) is necessary. The approximate forms, particularly in Eq. (10), are of quite limited validity, while the initial expressions are much more appropriate.

The expression for μ is given relative to μ_1 at normal incidence, to indicate the inverse cubic dependence of photoabsorption on energy away from the edges. The dependence on the Bragg angle bears little similarity to previously considered corrections, and also varies from low order to high order limits. Equation (11) indicates asymmetric diffraction through α_p. μ should include the mean effect of extinction (diffraction) prior to the depth involved. For flat crystals R_z is infinite, so the contribution of Eq. (10) is zero; but for near-flat crystals, this extinction can increase μ by orders of magnitude near the peak. For significantly curved crystals, the diffraction process is effectively negligible prior to the diffraction peak, and the inclusion of "flat crystal" values for extinction leads to errors of orders of magnitude in this correction.[17,18,38]

Corrections for profile asymmetry and attenuation (which depend on penetration depth) require estimates for F'_H and F''_0, respectively, so they are not amenable to the simplified Eqs. (3) and (4). More refined estimates of form and structure factors must be made if this precision is required. This shift is often larger than the refractive index correction and of opposite sign. Figure 10 considers the value of the approximate forms of Eq. (11) for low and high orders. Note the different regimes depicted. Use of the approximate Eq. (11d) is generally invalid, although the qualitative form becomes valid for high Bragg angles of ADP 101 0.4-mm-thick crystals (with the given 300 mm curvature). As the crystal thickness is reduced or the diffracting order is increased, Eq. (11c) becomes a more appropriate and accurate estimate over wide ranges of Bragg angles. Thus PET 008 diffraction penetration depths are well represented by Eq. (11c) for all angles, whereas this is far from true for PET 002. In all cases, penetration depth becomes more important in absolute and relative senses as the Bragg angle decreases. The potential uncertainty of the crystal thickness on the dependence of Eq. (11c) may be seen to be significant.

The use of Eq. (11a) with Eq. (10) is able to yield the correct result in the general case, but requires a valid linear absorption coefficient μ_{abs} together with an appropriate estimate of mean extinction μ_{ext}. The former can be evaluated and indicates the form of the dependence, but is typically a factor of 2 or so too small, depending on wavelength, curvature, thickness, and polarization. Figure 11 compares this estimate to those derived from dynamical theory for each polarization. The simpler estimate based on absorption is entirely adequate for PET 008 diffraction, except at normal incidence. For ADP 404, absorption estimates are excellent for much of the angular range, while at higher Bragg angles the increasing thickness of the lamellar diffracting units and
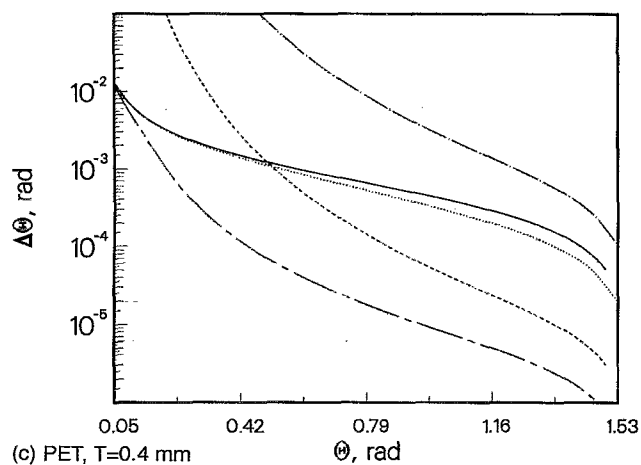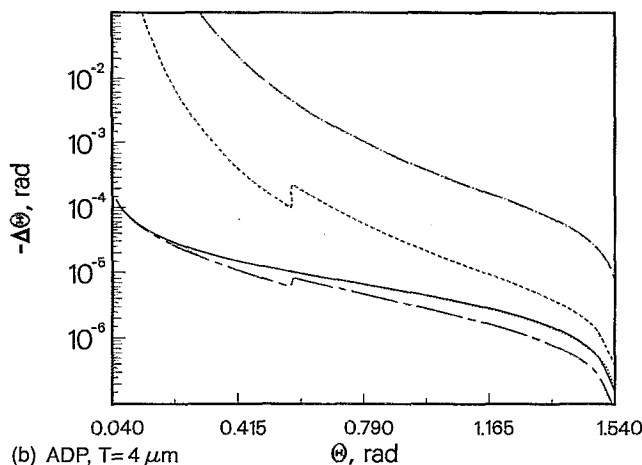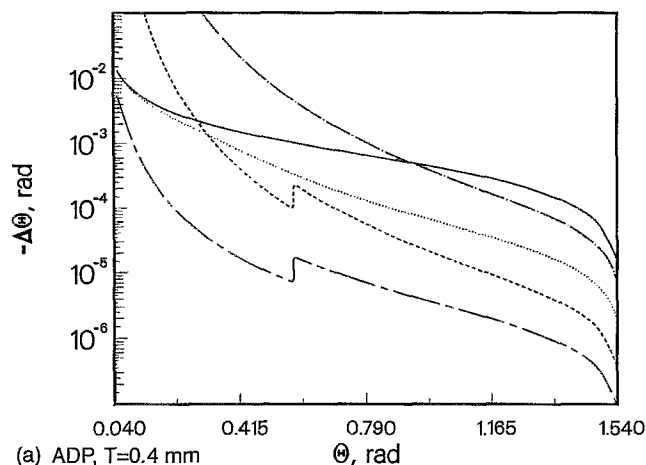
(a) ADP, T=0.4 mm Θ, rad

(b) ADP, T=4 μm Θ, rad

(c) PET, T=0.4 mm Θ, rad
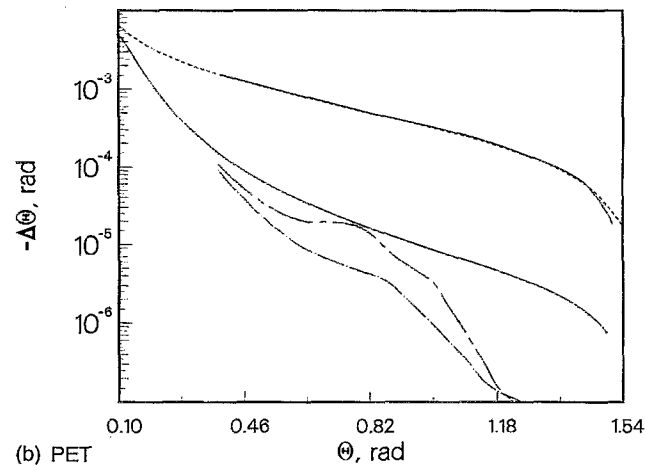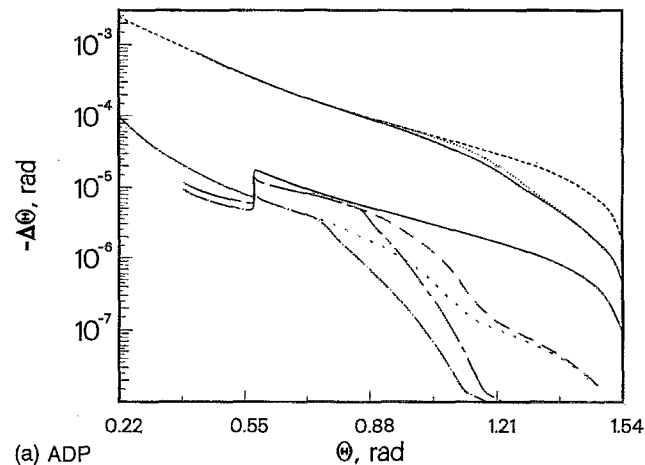

(a) ADP Θ, rad

(b) PET Θ, rad

FIG. 11. Estimates of centroid shifts due to depth penetration in curved crystals. Here the best of the previous estimates [Eq. (11a), lower solid curve for first order planes, dash for higher order planes] is compared to those obtained with Eq. (10) but using input $\bar{d}$ values including extinction, derived from dynamical calculations ($\cdot-,--$ for first-order planes and π or σ polarization, dotted and upper solid curves for corresponding polarizations in higher order planes; see the text). The low angle cutoff depicted represents the minimum diffracting angle for the source geometry chosen. The fall-off for first order diffraction at high angles is due in part to the small values involved and consequent computation difficulty in the dynamical calculations. (a) ADP 101 and 404 diffraction for $T=0.4$ mm, $2R_z=300$ mm. Different source and crystal dimensions are compared in diverging short dash and long dash lines from first-order curves at intermediate angles. (b) PET 002 and 008 diffraction for $T=0.4$ mm, $2R_z=300$ mm.

FIG. 10. Estimates of centroid shifts due to *depth penetration* in *curved crystals*. (a) ADP 101 and ADP 404 diffraction with crystal thickness $T=0.4$ mm, crystal radius $2R_z=300$ mm, estimating the shift of the exit angle at surface vs Bragg angle. The solid line represents Eq. (11c), and unsimplified Eq. (10); (—) and (--) give the infinite crystal limit [Eq. (11d)] and the better estimate of Eq. (11a) for ADP 101 diffraction; while ($\cdot-$) and ($\cdots$) give corresponding curves but for ADP 404 diffraction. Effects are larger for higher orders of diffraction and for lower Bragg angles. (b) The same as for 2 (a) for ADP with a crystal thickness $T=4$ μm. Now Eq. (11c) becomes a good approximation for ADP 101 and 404 over much of the angular range. (c) The same as for 2 (a) but relating to PET 002 and PET 008 diffraction. Equation (11c) is a good approximation for PET 008 for all angles, while the unsimplified formula is required for PET 002.

the near-flat nature of the crystal lead to reductions of the effective depth penetration by polarization-dependent factors of 2 or 3. For PET 002 and ADP 101 diffraction, extinction is significant even at low angles, reducing depth estimates by a factor of 2 or 3; while at higher angles the extinction rapidly dominates in the region of significant diffraction, thus reducing the expected depths by orders of magnitude.

Estimates using Eq. (11a) are best where the correction is large, and may be compared (favorably) to other estimates [Eqs. (11b)–(11d)] across the Bragg range. The correction is sensitive to absorption edges and increases (rapidly) toward low angles. Linear interpolation between calibration lines can yield high accuracy away from these regimes. The uncertainty in the mean extinction, and hence the effect of penetration depth, is primarily eliminated only by the use of
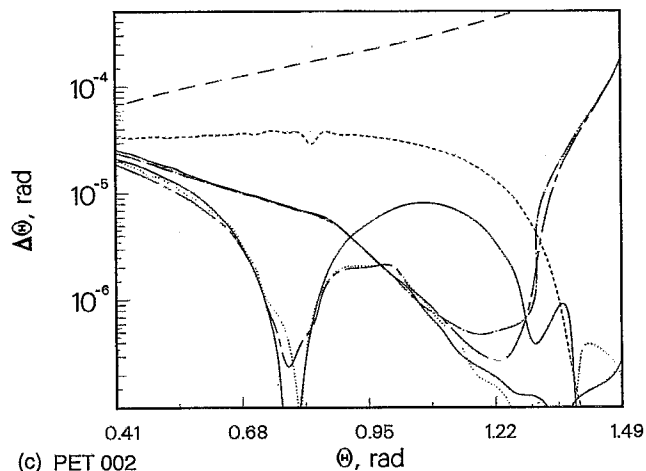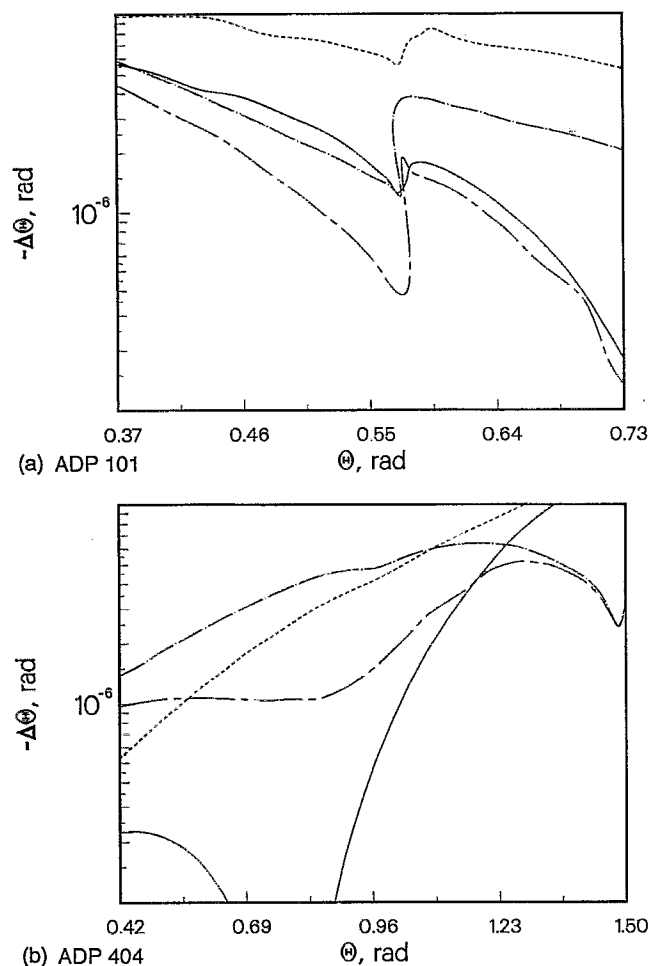
(a) ADP 101 Θ, rad

(b) ADP 404 Θ, rad

(c) PET 002 Θ, rad

FIG. 12. *Diffracting angle shift* estimates. (a) ADP 101 diffraction for $T=0.4$ mm, $2R_z=300$ mm. The simple estimates of Eq. (12) for π and σ polarizations (solid line and dash, respectively) is within a factor of 3 of the computed (dynamical) value (—–and ·—, respectively) below the absorption edge. At higher Bragg angles the agreement for σ polarization improves slightly while that for π polarization improves significantly, lying within 10% of the computed value despite the rapidly decreasing magnitude and some precision-dependent fluctuations. (b) ADP 404 diffraction for $T=0.4$ mm, $2R_z=300$ mm across the full angular range. Here the estimates and computed values are smooth and well defined but bear little relationship to one another. Note particularly the failure of Eq. (12) for σ polarization between 35° and 55° and other discrepancies by an order of magnitude. (c) PET 002 diffraction for $T=0.4$ mm, $2R_z=300$ mm showing the complexity of estimates and calculations. In addition to the previous curves, the dotted and solid lines converging at normal incidence indicate σ and π polarization computations evaluated over the full width at 1% of the peak reflectivity, while the long dash at the top of the curve represents the total (π) correction. Except for this last curve, all shifts are negative, as in (a) and (b).

dynamical calculations.[17–19] While these equations are reliable estimators, and the figures provide a useful comparison of these equations, it is also useful to provide some typical magnitudes, as indicated in Table III, for comparison with flat crystal and other effects. The latter should be considered unreliable in comparison to the former, but may be a more useful and direct presentation for researchers considering the importance of component effects.

D. Mean angle of incidence on diffracting planes for curved crystals

There is a second contribution to the mean output angle, due not to the penetration depth but to the transmission-averaged mean diffracting angle. This arises because low incident angles will not yield a mean angle based on flat crystal reflectivities. Instead, the x rays are attenuated as they penetrate the crystal. Often before the flat crystal profile peak $y \simeq -1$ is reached, the transmission will become negligible. Thus a potentially large shift to lower angles results.

For low absorption and narrow (high-order) diffraction profiles, this is generally a small effect, perhaps a few percent of the depth penetration estimate discussed above. However, for highly absorbing and wide (first-order) diffraction profiles, this can often be 50% or more of the shift due to the mean depth, with the same sign. The magnitude depends

critically on the curvature, since transmission coefficients are dependent on the effective layer (or lamellar) thickness. In these cases it is difficult to neglect this contribution.

Since the effects of depth penetration and curvature are of similar orders of magnitude and are interrelated, it is difficult to isolate reasonable estimates for consequent shifts without pursuing full dynamical calculations (as indicated in Sec. III C). However, an estimate may be made using only the flat crystal profile for the appropriate effective thickness, combined with an estimate of the angular shift between adjacent layers in the curved crystal. Then

$$\Delta\theta_T \simeq \frac{\Sigma_i \theta_i r_i t_i^{2/n}}{\Sigma_i r_i t_i^{2/n}} - \theta_P, \tag{12a}$$

$$n = \frac{\Delta y_0}{\Delta\theta_f}\left(\frac{-2b\cos\theta\sin\theta_B}{\sqrt{|b|}|C\psi_H'|}\right), \tag{12b}$$

where $\Delta\theta_f$ is the shift of $\theta_{i+1}-\theta_i$ between adjacent steps i of the computation of the flat crystal profile reflectivity and transmission coefficients r_i, t_i; θ_P is the mean angle of the asymmetric flat crystal profile; and Δy_0 is an estimate of the shift in the diffraction coordinate y through the lamellar thickness. This estimate is often 2 (corresponding to the Darwin or nonabsorbing full width), but can be much larger where the curvature radius is small, particularly for first-

TABLE III. Magnitudes of corrections relative to refractive index shifts: Typical estimates for curved crystals.

Factor	Application	Percentage	Sec.
Asymmetric diffraction, 1°	Angle to surface[a]	2%–7%	III B
	Exit vs incident angle	0.1%–1.0%	
Flat crystal peak shift	Thick perfect crystal	10%–50%	III B
	Very thin or ideally mosaic crystal	0%	
Form factor uncertainties	Generally	0.1%–1.0%	III B
Possible three-beam interaction	Allowed, low order, high angle	0%	III B
	Allowed, low order, medium angle	1%–20%	
	Allowed, medium order	10%–200%	
	Forbidden	5%–100%	
Depth penetration	Low order, high angle	0%–10%	III C
	Low order, low angle	10%–100%	
	Medium order, high angle	>100%	
	Medium order, low angle	>1000%	
Mean angle of incidence	Low order	0%–50%	III D
	Medium order	10%–100%	
Off-axis shifts	High angle (low order)[b]	>100%	III E
	On axis	0%–10%	
	Low angle (low order)[b]	>1000%	
Lateral shifts	High angle, low order	0%–5%	III F
	Low angle, low order	10%–100%	
	High angle, medium-order	1%–50%	
	Low angle, medium-order	>1000%	
Source and crystal lengths		0%–20%	III G–III J
Crystal and source heights		10%–200%	III K
Emulsion (detector) shifts		1%–100%	III L
d-spacing shifts	Low order	0%–10%	III L
	Medium order	0%–400%	

[a]After correction for α_p itself.
[b]Much higher for higher orders.

order radiation. Then the lamellar thicknesses, equivalent to mean coherence lengths, significantly broaden the profile width (on the diffraction coordinate or other scale).

This (simple) estimate is compared in Fig. 12 to a mean angle with respect to diffracting planes summed over an assumed source distribution and a diffracting crystal, following dynamical theory with certain approximations. The computation includes small (tertiary) corrections due to the crystal thickness and length limits, which truncate reflectivity profiles at extreme angles. The source distribution is focused by the crystal so that the reflectivity on the diffracting Bragg angle scale may not follow a linear relation compared to that for the source distribution. In recommended geometries, this nonlinearity is usually negligible but would also be accounted for in the latter procedure. The two results are often in agreement within a factor of 3, particularly at the low Bragg angles where the shifts are most significant. Above the PK edge for ADP 101 diffraction, σ polarization estimates and computation agree within 10%, despite computational limitations near this level.

However for ADP 404 [Fig. 12(b)], the result of Eq. (12) and the computation both indicate increasing shifts with Bragg angle, but with quite different functional forms and magnitudes. Equation (12) fails for σ polarization at around 45° because of the negligible transmission coefficient, and at near-normal angles because of the large lamellar unit. In all cases, Eq. (12) is strictly valid (in the approximate sense) only for iteration outside a lamellar unit, i.e., if n approximates unity. For an n significantly larger than unity with significant extinction through a lamellar unit, the component

relating to intraunit averaging does not behave like Eq. (12a) (the amplitudes add coherently and in phase). The peculiar behavior of the computation in Fig. 12(b) in the neighborhood of normal incidence correlates with the decline in depth penetration and the change of angle with depth, reversed as the high-angle portion of the profile (not contributing to the angle shift) is truncated at 90°.

Additional complexity for PET 002 is provided by Fig. 12(c). When the magnitude of the shift falls below 10^{-6} rad, computational precision introduces large relative but negligible absolute uncertainty. Further, results below 60° are dominated by the central portion of the diffraction profile (above 1% of the peak reflectivity), whereas the effect of the diffraction wings or tails is significant for Bragg angles above 75°, leading to increased sensitivity to source and crystal dimensions (Secs. III C–III K).

The detailed correction is compared to other contributions and the resulting (calculated) mean angle in Fig. 13 to indicate the typical good agreement of these contributions with the total. Typical component magnitudes are illustrated in Table III (neglecting the detailed and complex angular dependence and functional form).

E. Off-axis diffraction for curved crystals

The mean angle resulting from flat crystal effects and depth penetration contributions varies around the crystal surface, and originates at different locations. Ideally (i.e., at the pole axis), these sources converge in the Rowland circle geometry to yield Eq. (5d), as indicated in Table II.
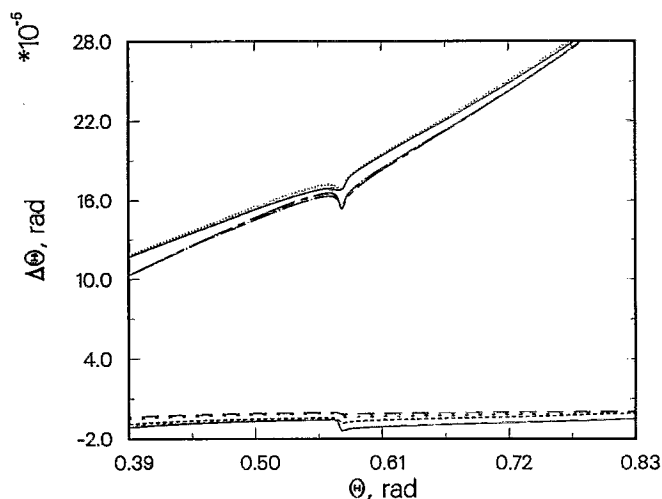
FIG. 13. (a) Sums of contributions to *mean exit angle* at the surface of the curved crystal [mean exit angle (curved crystal)=mean exit angle (flat crystal) + D.P. angular shift + mean diffraction angle shift]. The solid and dashed lines at the bottom are (negative) depth penetration (D.P.) corrections for σ and π polarizations. (--) and (·-) give total mean angular shifts, while the upper curves (dotted and solid, respectively) give the mean angular shift for the corresponding flat crystal (with a thickness corresponding to the region of coherent excitation with significant amplitude, and hence to the curvature). (-··) and (···) indicate related diffraction angle shifts. ADP 101 diffraction for $T=0.4$ mm, $2R_z=300$ mm. The flat crystal result dominates, with up to 20% corrections due to the mean penetration depth and up to 10% due to the mean diffracting angle shift, both decreasing with increasing Bragg angle.

However, for most spectrometers observing a significant range of wavelengths simultaneously (across a detector), the effects of the previous sections are normally highly correlated with shifts due to the location of diffraction lying away from the pole axis (cf. Fig. 9). The first-order effect of this is to reduce arc lengths Y_z around the Rowland circle below $2R_z\theta$ by a percent or so, following the estimate

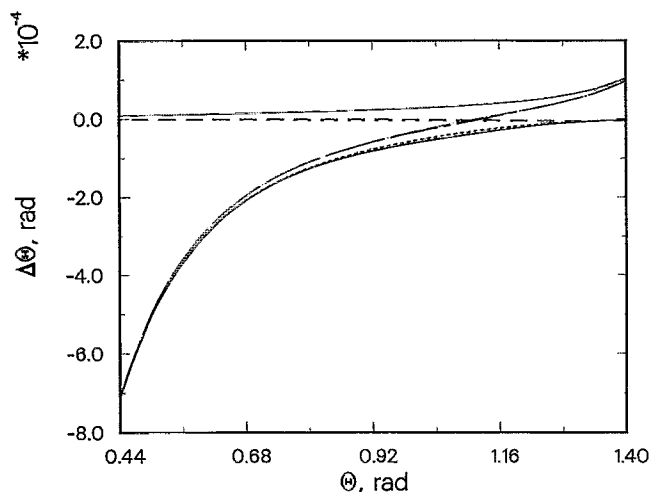$$\Delta Y_z \simeq -R_z \cot \theta_{\mathrm{out}} \sin^2 \theta_A, \tag{13a}$$

FIG. 13. (b) ADP 404 diffraction for $T=0.4$ mm, $2R_z=300$ mm. The mean penetration depth provides the dominant contribution except at near-normal incidence, σ and π polarization curves are barely distinguishable, and the diffracting angle shift remains the smallest contribution.
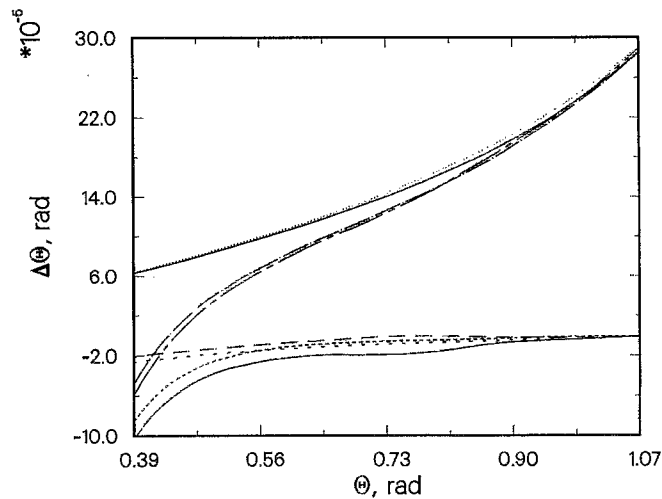
FIG. 13. (c) PET 002 diffraction for $T=0.4$ mm, $2R_z=300$ mm. The diffracting angle shift provides an 18% correction to the flat crystal shift for much of the angular range, while the mean penetration depth and flat crystal shifts are of a similar magnitude.

$$\theta_A = \frac{XP}{2R_z}, \tag{13b}$$

where XP is the arc length of the peak (mean) diffraction along the generatrix of the diffracting crystal to the pole axis (the amount by which the diffraction is off axis). (The generatrix is the plane normal to the axis of the cylinder and passing through the center of the crystal, as illustrated in Fig. 9.) θ_A depends on the source geometry and alignment, as a function of θ_{out}. This function $\theta_A(\theta)$ is the same if $\theta=\theta_{\mathrm{out}}$ is replaced by $\theta=\theta_B$ or $\theta = \theta_B + \Delta\theta_{RI+\text{profile } a/s}$. Hence just as Y_z is here related to θ_{out}, so Y_B can be related to θ_B, while shifts of θ can be related to shifts of Y_z.

The off-axis shift is zero where the crystal is tangential to the Rowland circle [38° for the geometry selected in Fig. 14(a)], and also disappears at normal incidence. A peak shift is therefore obtained at an intermediate angle (around 63°), with a larger shift at minimum diffracting angles. Although $\Delta Y_z = Y_z - Y_B$ is found to be linear in $\Delta\theta$ for each of the systematic corrections to θ (except near the pole), the linearity is often far from $2R_z$ and can reach a ratio of $3R_z$ in typical cases. A point source B at a distance BP from the pole (cf. Fig. 9) and with a grazing incidence angle θ_{Ax} to the surface at the pole leads to a minimum grazing incidence angle around the crystal circle

$$\theta_{\min} = \arccos \sqrt{1 - \frac{BP}{2R_z}\left(2 \sin \theta_{Ax} - \frac{BP}{2R_z}\right)} \tag{14a}$$

and

$$\theta_A = \arcsin\left(\frac{\cos \theta_{Ax}}{\cos \theta_{\min}}\right) - \arcsin\left(\frac{\cos \theta}{\cos \theta_{\min}}\right) - \theta_{Ax} \pm \theta, \tag{14b}$$

where θ_A is measured in an anticlockwise direction, the positive sign on θ refers to most geometries, and the arcsin terms could fall within either $(0, \pi/2)$ or $(\pi/2, \pi)$ ranges, depending on the geometry. Assuming symmetric Bragg diffraction at the surface yields $\theta_{\mathrm{out}}=\theta$. This then specifies the relation
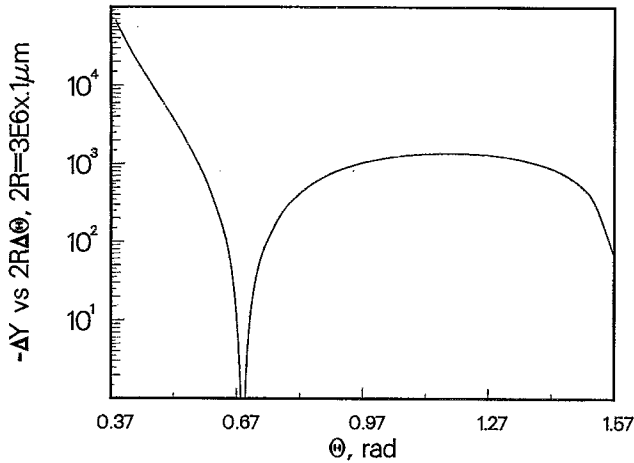
FIG. 14. (a) Off-axis corrections and the effect on the proportionality of depth penetration and other shifts on the detector location on the Rowland circle. The difference between the location of detected radiation (assuming diffraction at the Bragg angle at the crystal surface, for a point source) and Eq. (5d) is indicated for ADP 101 diffraction in a typical geometry. Equations (13) and (14) effectively reproduce this dependence.

FIG. 14. (b) The shift from the Bragg angle to the mean diffracting angle for flat crystals for σ and π polarizations and ADP 101 diffraction, scaled by $2R_z$ (solid and dashed lines), is compared to calculated positions in the in-circle geometry (– – and ·–·–) and the on-circle geometry of the text (·). The latter reproduce results of Eqs. (13) and (14) on this scale. While in-circle results are conveniently interpreted as significant proportionality errors with appropriate corrections, the magnitude and sensitivity of on-circle corrections is not easily combined into this approach.

of θ_A to θ or θ_{out} and allows explicit estimation of the effects of mean angular shifts (refractive index corrections, profile asymmetry, nonalignment of diffracting planes, and mean shift of the surface angle due to depth penetration) on the detector position on the Rowland circle.

The effect of off-axis corrections on the proportionality of shifts along the Rowland circle compared with the angle is indicated in Fig. 14(b). For low angles with the source well inside the Rowland circle, this is particularly significant, while shifts of a percent or more persist at quite large angles. For a source centered on the Rowland circle, the effects are much larger. This can distort relative measurements or minimize their sensitivity, unless each wavelength (or spectral line) is scanned to optimize the intensity as a function of source position.

F. Lateral shifts due to depth penetration

A shift of the exit location of the ray also arises due to the penetration depth: this causes a transverse shift for flat crystals, dependent on μ including extinction near the profile peak. For curved crystals at the pole axis the shift of position at the detector may be estimated as

$$\Delta Y_l(A,B) \simeq R_z \arccos[(2 \cos B - \cos A)\cos A$$

$$- \sqrt{\sin^2 A(\sin^2 A + 4 \cos^2 B - 4 \cos B \cos A)}]$$

$$\sim 2R_z B, \qquad (15a)$$

$$B = \theta_B + \alpha_p, \quad A = B + \theta_A, \quad \theta_A = \Delta\theta_{in} + \Delta\theta_{out}, \qquad (15b)$$

where the last quantities are given by Eq. (10); or, less precisely,

$$\Delta Y_{l,0} \simeq - R_z \cot \theta_{out} \sin^2 \theta_A, \qquad (16a)$$

$$\sin\left(\frac{\theta_A}{2}\right) \simeq \max\left(\frac{XP}{4R_z}, \frac{XZ}{4R_z}\right),$$

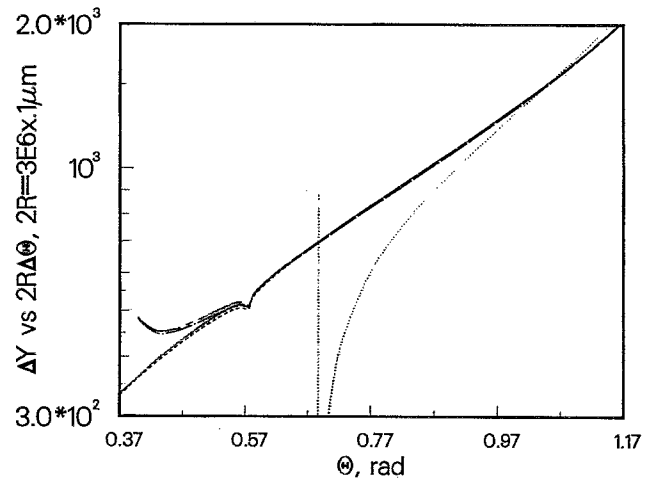$$XZ \simeq \bar{d}[\cot(\theta_B + \alpha_p) + \cot(\theta_B - \alpha_p)]$$

$$\simeq 2\bar{d} \cot \theta_B, \qquad (16b)$$

where XP follows Eq. (13b) (Fig. 9). A slight imprecision of the alignment of thin crystals on the Rowland circle, or the simultaneous observation of a wide angular range (using calibration lines from a broad source, for example), leads to an XP of the order of 1–10 mm, dominating over XZ in Eq. (16). This then includes intrinsic shifts and defocusing from the off-axis position of diffraction on the crystal. Whereas the use of XZ in Eq. (16b) or Eq. (15b) estimates the minimum (and negligible) off-axis correction, the use of XP in Eq. (16b) may be set to the crystal length to estimate the maximum (off-axis and lateral) correction. Alternatively, the lateral estimate can be isolated from angular shifts due to depth penetration using

$$\Delta Y_{lat} = \Delta Y_l(A_1, B) - \Delta Y_l(A_2, B), \qquad (16c)$$

$$B = \theta_B + \alpha_p, \quad A_1 = B + \theta_A - \Delta\theta_{in} - \Delta\theta_{out},$$

$$A_2 = B + \theta_A, \qquad (16d)$$

where A_2 is derived from the extreme angle $\theta_A = \theta_{A,max}$ defined by the size of the diffracting crystal and A_1 is derived from this maximum value of XP (or θ_A) minus the lateral shift XZ (or $\Delta\theta_{in}$, $\Delta\theta_{out}$). These extreme estimates are indicated in Fig. 15(a), scaled to show changes in the effective Bragg angle. The estimates vary from dominating over refractive index corrections and other flat crystal contributions, to being less than 1 ppm over the full angular range. The last estimate, following Eqs. (16c) and (16d), is a useful overestimate for comparison to other contributions.

Using the same equations, with θ_A provided from an experimental geometry [Eq. (14b)] gives a more realistic result, sensitive to the sign of the lateral shift. A more accurate estimate would separate the angular depth penetration correction
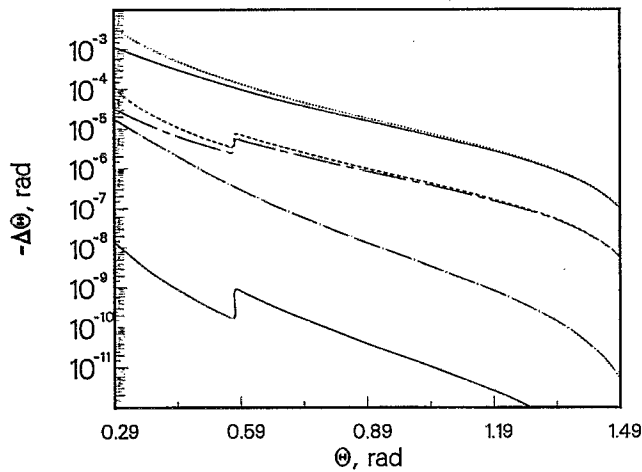
FIG. 15. (a) Estimates of *lateral detector shifts*. Upper and lower limits in magnitude are presented for ADP 101 and ADP 404 diffraction with $T=0.4$ mm, $2R_z=300$ mm. The use of XZ in Eq. (16b) or the use of Eqs. (14) and (15b) generates the lower two curves for on-Rowland circle shifts, while setting XP to an assumed crystal length generates the dotted and dashed curves, compared to the somewhat reduced maxima following Eqs. (16c) and (16d). These limits represent typical ideally aligned or ideally misaligned shifts. Shifts of the opposite sign would occur for misalignment on the opposite side of the pole axis of the crystal. Maximum shifts for ADP 404 are several thousand ppm at low angles, while even near normal incidence these effects can be of the order of 1% of the flat crystal corrections.

$$\Delta Y_{DP}=\Delta Y_l(A_2,B_2)-\Delta Y_l(A_1,B_1), \tag{17a}$$

$$B_1=\theta_B+\Delta\theta_{RI+Profile\ a/s}, \quad B_2=B_1+\Delta\theta_{out},$$
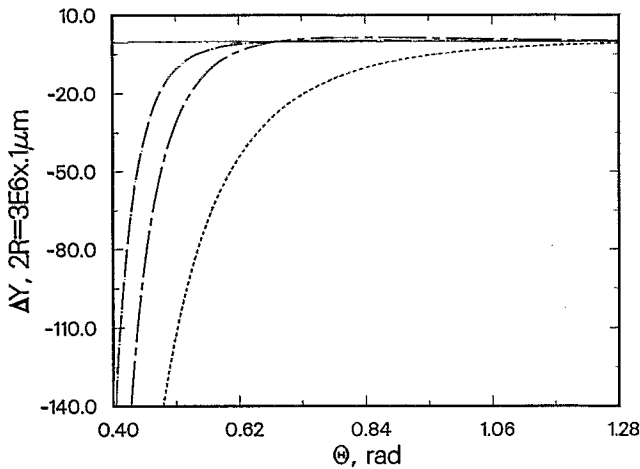
$$A_i=B_i+\theta_A(B_i), \tag{17b}$$

FIG. 15. (b) Shifts at the *detector location* (on the Rowland circle) for PET 002 diffraction in the geometry indicated earlier. The ideally aligned and ideally nonaligned estimates of magnitude are indicated by solid and dashed lines, respectively. The curve — represents the use of Eqs. (16c) and (16d), (14b), (10), and (11a), with μ provided by the absorption coefficient only. It represents the application of the earlier (relatively straightforward) estimates to the "real" in-circle geometry, with the same assumptions regarding attenuation. Note the change of sign just prior to the Bragg angle where the crystal lies ideally aligned on the Rowland Circle. By contrast, (·–) uses Eqs. (17b), (18), (10), and (11a), with the effective μ including computed mean extinction for π polarized radiation, and hence is the best estimate of the lateral shifts for a given geometry. The simpler estimate is well able to indicate the magnitude and sign of the correction, but for precise quantitative corrections to effective angles or wavelengths it is inadequate, whether at the 100 ppm level for low angles or at the 1 ppm level for high angles.
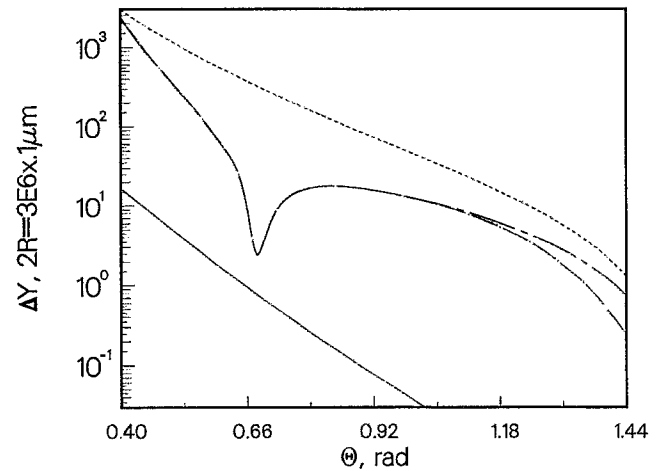

FIG. 15. (c) Absolute magnitude of shifts at the *detector location* (on the Rowland circle) for Si 444 diffraction in the geometry indicated earlier. The curves have the same meaning as in Fig. 14(b). Here the simpler estimate provides the correct detailed correction, except at high angles, despite the shifts being much larger than in Fig. 14(b).

from the lateral shift

$$\Delta Y_{lat}=\Delta Y_l(A_3,B_2)-\Delta Y_l(A_2,B_2), \tag{18a}$$

$$A_3=B_2+\theta_A(B_2)-\Delta\theta_{in}-\Delta\theta_{out}. \tag{18b}$$

In these cases, $\theta_A(B)$ is given by $\theta_A(\theta)$ in Eq. (14b).

It is perhaps surprising that such large effects arise from these angular and lateral shifts (Fig. 15). They vary from insignificant (the aligned, on axis estimate for lateral shifts) to significant at most angles (depth penetration estimates) to dominant at particular low grazing angles and potentially large elsewhere (extreme off-axis estimates for lateral shifts). It is necessary to use the best estimates to hope to reach agreement within a factor of 2 of the true shifts. One difficulty relates to the need to include explicitly the off-axis nature of the shifts at the detector, rather than using maximum or minimum values. A second relates to the difficulty in evaluating the mean extinction addition to the linear absorption coefficient. For a quick estimate, μ_{abs} may be calculated explicitly, and (for curved crystals) μ_{ext} may be neglected. This typically yields overestimates of depth penetration, and hence of the associated angular and lateral shifts, by factors of 2–3. For high orders of diffraction, the associated error can be negligible in appropriate crystals, angles, and energies.

For a small but finite source inside the Rowland circle and arbitrary crystal dimensions, these effects sum to yield the total centroid shift of a profile entering a detector on the circle. Often the associated precision can lie at or below 1% of the corrections to the Bragg relation, although some components may only be accurate to a factor of 2 or 3 if the above simple formulas are used.

G. Finite dimensions and geometric corrections

Other effects due to the Johann geometry and finite sources are ray tracing exercises, which can give significant

modifications of on-Rowland circle relations and more complex off-Rowland circle effects with a consequent variation and distribution of shifts.

The source should ideally be well centered with respect to the (cylindrical) crystal curvature and the central plane of the crystal and the detector location. Nonalignment of the source with the central plane of the crystal generatrix leads to broadening and shifts dependent on the height of the source and crystal and the detector resolution in the transverse direction. Formulas for some of these have been discussed elsewhere,[37,39–42] and have an origin which is primarily external to the crystal. These references neglect attenuation, extinction, and diffraction profiles, and assume that the diffraction profile width is significantly larger than the spread of grazing angles at and inside the crystal (both in simple analytic formulas and in deconvolved numerical procedures). The formulas and numerical calculations locate the crystal on the Rowland circle at the Bragg angle to the source for all wavelengths considered, with the source center also on the Rowland circle.

They provide estimates of centroid shifts due to finite crystal and source size. However, additional terms typically arise [cf. Eq. (18) of Ref. 40] which may dramatically modify the effective shift. A source location well inside the Rowland circle leads to a range of θ_i far in excess of the crystal diffraction width, so that the mean shift must be significantly truncated or modulated. Finally, the normal procedure of comparing spectral lines imaged with a curved crystal allows only one (monochromatic) wavelength to be imaged at the crystal pole axis with $\theta_B = \theta_{Ax}$, while the other wavelengths necessarily follow an off-axis relation. At least some of this inconsistency or lack of applicability has been noted earlier.[41] By comparison, the program discussed in Refs. 17–19 takes explicit account of the off-circle relations and includes broadening, convolutions, and shifts from finite source widths and depths, and finite crystal widths and depths.

H. Crystal length along the generatrix

This was discussed from a different perspective for a particular case in Ref. 38 and may be addressed by considering Fig. 14(a). Here the grazing angle at the pole axis was defined to be $\theta_{Ax} = 0.687\,677$ rad, with an in-circle point source of $BP = 26$ mm from the pole axis and a crystal radius of $2R_z = 300$ mm. If $\theta_B = \theta_{Ax}$, then the detector locations for wings on both sides of the Bragg angle shall be reduced by the amount indicated. (Of course, it would be more appropriate to use $\theta_P = \theta_{Ax}$.) The mean of these angles (modulated by some reflectivity and angular source distribution) would be shifted strongly to lower apparent angles (and wavelengths) by the steep slope on both sides. At θ_{Ax}, this appears quadratic in θ and hence quadratic in the corresponding crystal length position along the generatrix.

If $BP = 2R_z \sin \theta_{Ax}$ (the source also on the Rowland circle) and the spread of grazing angles along the crystal length t_0 is significantly less than the rocking curve width, then the standard formula

$$\frac{\Delta \lambda}{\lambda} \simeq \frac{t_0^2 \cos^2 \theta_{Ax}}{24(2R_z)^2 \sin^2 \theta_{Ax}} \tag{19a}$$

is an accurate description of the additional *mean grazing angle shift* (at the surface or equally at the diffracting planes). For a crystal radius $2R_z = 300$ mm and $\theta_{Ax} = \theta_P = 0.687\,677$ rad, the range of significant diffraction (for ADP 101 planes) occurs over a 5 mm crystal length, although the profile FWHM is 3 mm. The grazing angle at the pole axis is also the minimum angle subtended by the point source on the Rowland circle, so that only the portion of Fig. 14(a) above $\theta = \theta_{Ax}$ would exist, and would be bimodal (with one curve for contributions from the parts of the crystal closer to the source and one curve for contributions from the other half). However, the *detected location* of these tails is shifted to apparently *lower* angles by *large off-axis corrections*. The two effects approximately cancel to within 1% of their magnitude. By comparison the simple estimates given above for depth penetration and mean angular shift (as opposed to detailed calculations) were only generally accurate to a factor of 2 or 3, or some 100 times this uncertainty. The separation of shifts due to changes in surface grazing angle from those due to lateral or off-axis shifts, seen in earlier sections, is less valid here as the diffracting region covers a large range of surface angles and locations, and those points with the largest (positive) angular shifts are also those with the largest (negative) off-axis shifts.

Equation (5d) (see Table II) becomes quite invalid and the scaling of off-axis shifts implies that detector shifts of 1 μm can represent a diffracting angular change of 100 ppm. This may be a real angular shift, but may also arise from very small lateral shifts due to depth penetration. Consequently, the interpretation of centroid and profile results is nontrivial. Therefore, the observed angle is extremely sensitive to the spectrometer alignment, since a change of minimum diffracting geometry $\Delta \theta_{min}$ to higher angles [from a change in the source location, pole axis angle, or crystal radius, as indicated in Eq. (14a)] leads to a direct and near-equal shift in the apparent or detected mean diffracting angle (and likewise in the peak angle). The off-axis correction will also change; the mean can appear to first-order as the minimum spectrometer angle θ_{min}, whether the flat crystal peak angle θ_P is greater or less than this. A second-order correction depends on the asymmetry of the portion of the flat crystal diffraction profile actually diffracted, compared to the asymmetry and scale of the off-axis shifts. The reflectivity will drop as θ_{min} approaches or exceeds θ_P.

The several hundred ppm magnitude of this potential shift, and its extreme sensitivity, imply that precision measurements of this type are not feasible without a careful modeling of the profile and the intensity and extreme precision of alignment. Typically, relative measurements will utilize a secondary source of x rays at a different physical location compared to the unknowns being measured. The variation of location in this nearly on-circle geometry can lead to large systematic shifts of the type just mentioned, so that the difficulties in interpretation remain in these types of measurements.

For the in-circle geometry with $t_0 = 14.6$ mm, Eq. (19a)

underestimates the range of grazing angles and hence the shift. One side of the crystal now corresponds to lower grazing angles but the symmetry around the pole of the off-axis shifts is maintained. Despite the angular range extending 5–10 or so times the on-Rowland circle estimate, off-axis shifts at the extremes are similar, modulated by less than a factor of 2. For sources either on or off the Rowland circle, a crystal dimension above $t_0 = 14.6$ mm clearly reveals the nonquadratic relation of the off-axis contributions, further reducing the overall centroid shifts.

More significantly, the effective range is generally strongly modulated by the (much) narrower diffraction width. For the (typical) example of ADP 101 diffraction, the FWHM for flat crystal diffraction is 3.2×10^{-5} rad, while the broadened width on the surface output angle profile at the pole axis is still only 3.8×10^{-5} rad and the 1 percentile range is only 3×10^{-4} rad. Following Eqs. (13b) and (14b), the latter range corresponds to a crystal length of 0.018 mm for the surface; allowing for broadening due to depth penetration down to the 5% level raises this to only 0.04–0.05 mm. This is in good agreement with the following, simplified form of Eqs. (13b) and (14b):

$$
\Delta XP \simeq \begin{cases}
2R_z\sqrt{2\,\sin\Delta\theta_w\,\tan\theta_{Ax}}, \\
\\
\quad\text{source on Rowland circle;} \\
\\
2R_z\Delta\theta_w\left(\dfrac{\sin\theta_{Ax}}{\sqrt{\cos^2\theta_{\min}-\cos^2\theta_{Ax}}}-1\right), \\
\\
\quad\text{source well inside Rowland circle}.
\end{cases} \quad (19b)
$$

Quadratic or other effects outside this range are simply irrelevant (as confirmed in tests). At this 5% extreme (± 0.02 mm), the expected off-axis shifts at the detector are approximately -0.0483 and -0.0376 μm at lower and higher angles, respectively; weighting this with the relative intensity one might expect a mean shift of -0.005 μm or an effective angular shift of 10^{-9} rad! This is certainly negligible compared to all other shifts discussed earlier.

For a diffracting angle peak some 0.08 rad away from the pole axis [cf. Fig. 14(a)], a linear variation of detector shift with angle (or crystal location) occurs so that the mean centroid shift from off-axis shifts would be precisely zero. Additionally, for $\theta_B = 1.15$ rad, a broader quadratic minimum would lead to a mean shift of opposite sign and a greatly reduced magnitude, but with a large off-axis offset relative to the ideal [Eq. (5d)]. For the source well within the Rowland circle, as in the standard examples of this paper, diffraction at θ_P yields a significant total off-axis shift if the peak angle does not correspond to the grazing angle at the pole axis, θ_{Ax}. However, the crystal length around the generatrix contributes negligible shifts, which in addition are defined by the diffraction widths and not by the crystal dimension.

This fails to be true for a small source *very* close to the Rowland circle, where the profile is truncated at lower angles by the alignment and at higher angles by the diffraction width (or the crystal dimension). Even here, the upper angle *truncation shift* is typically only 10%–20% of the *mean shift of the diffracting angle*, and the *off-axis shifts* compensate

for this down to below 1% of the total shift from $\theta_{\min}$, or toward the ppm level. A more serious problem arises from the potential inequality of $\theta_{\min}$ and θ_P in this on-circle case, and the corresponding profile truncation.

Scanning methods are not uncommon in Johann spectrometers and optical elements, and lead to the possibility that a broad detector may be used instead of one with positional sensitivity. In this case, the spectrometer angle will define the reference position and the mean diffracting location, while complications of the focused profile are no longer of prime importance. If the (point) source is scanned around the Rowland circle relative to the pole axis of the crystal, then the diffracted intensity of a monochromatic wavelength will not be at maximum at the expected θ_P position. Instead, as discussed, the maximum will arise when the angle to the pole axis is less than this, so that two images are focused to the detector, one from each side of the pole axis. As the angle to the pole axis is decreased, the images will retain almost constant diffracted intensity as the diffracting regions of the crystal move further away from the pole. Finally, the diffracted intensity will drop rapidly as the images track beyond the crystal limits.

In other words, a normal finite curved crystal in a scanning on-circle geometry will have a high reflectivity from above the peak of the flat crystal curve (measured with respect to the pole axis) to a limit given by the edge of the crystal. Nonmonochromatic incident radiation widths will broaden this further. This profile is very broad and poorly centered due to the on-circle geometry, and hence does not avoid the difficulties discussed above.

I. Crystal and source depths

The effect of crystal depth in Refs. 40 and 42 is primarily an estimate of the lateral shift component for the source and crystal both centered on the Rowland circle [similar to Eq. (16a) using XZ in Eq. (16b)]. The integration was apparently performed over positive and negative depths (i.e., including regions outside the crystal). In the above in-circle geometry with a 0.4 mm depth, the quoted effect of crystal depth would be -0.066 μm at the detector or -2.2×10^{-8} rad. This is negligible. The prediction of the formula would be reduced dramatically by absorption and extinction coefficients as discussed earlier. This geometric component per se is inseparable from the aforementioned components defined by the mean surface angular shift upon depth penetration, the mean lateral shift upon depth penetration, the depth component of the mean diffracting angle shift, and even the effective mean shift of the flat crystal profile. These dominant contributions are large and significant in many cases, are often limited by the crystal depth, and are detailed in Secs. III C–III F.

Other references have been concerned with profile widths rather than shifts,[43,44] but provide useful expressions concerning these, particularly in the context of Sec. III L.

The source depth was correctly observed to have a negligible effect on centroid location, although the main effect would be to reduce shifts arising from the crystal length by providing more off-axis contributions with $\theta_P \neq \theta_{Ax}$.

J. Source length along generatrix

The quoted effect of source length along the generatrix (with a point crystal of negligible dimension) from Ref. 40 is the transform of a uniform range of $\Delta\theta$ (at the crystal surface) to a nonuniform range of $\sin\theta$. This corresponds to locally symmetric source geometries, uniform in the 2π angular distribution. Alternate nonuniform distributions can be significant and should be modeled separately to estimate this effect. Part of the effect for a symmetric distribution would be truncated by the diffraction width defining the effective source dimension if the latter were large enough to provide a significant shift. Unlike Sec. III I, there would be no off-axis correction at the crystal to compensate for this angular shift. Hence, if the location on the detector were transformed to a value of $\sin\theta$, the mean of the resulting profile could indeed be shifted significantly. However, the detector would typically either be a curved or flat plate on the Rowland circle or at some angle to it (e.g., normal to the ray from the pole axis). In this case, the profile on the detector, either ideally or otherwise, represents a profile in θ, as discussed earlier. Hence the centroid of such a profile would be *unchanged*.

The assumption of a point crystal is unrealistic, and the source length can couple with the crystal length and with the crystal depth (if, as in high orders of diffraction, absorption is negligible). For ADP 101 diffraction in the above examples, the mean penetration depth is only 3–5 μm, so that this coupling will not generate large effects.

If the angle subtended by the source $y_0/(2R_z \sin\theta)$ is greater than the diffraction width corresponding to the crystal length, estimated by inverting Eq. (19b) and replacing ΔXP by t_0, and with t_0 comparable to or less than the equivalent length for the diffraction width ΔXP [$\simeq$3–5 mm in the previous example, following Eq. (19b)], then rays from each pair of symmetric source points will cover higher and lower diffracting angles with equal intensity and approximately the same lateral shifts, so that $\Delta\theta_{\text{out}}$ and the mean detector location will be largely unaffected. [The detailed result, illustrated in Fig. 11(a), is dominated by varying truncation of the flat crystal profile and their effect on depth penetration, and small asymmetry in the truncation limits to yield a mean diffracting angle shift, corresponding to 1 μm shifts on the detector or 2 ppm effects in both in-circle and on-circle examples.]

Conversely, if the angle subtended by the source at the crystal is much less than the range of grazing incidence angles across the crystal (for a point source), and with both of these greater than the diffraction width $\Delta\theta_w$, then rays from each source point will cover the range of angles within the diffraction width, so that $\Delta\theta_{\text{out}}$ will be largely unaffected. However, diffraction will occur at crystal points far removed from the pole axis, so that the lateral off-axis shifts shall be just as large as in Sec. III H. For the typical in-circle example, the angle subtended by the source $y_0/BX\simeq y_0/BP$ and the range of angles across the crystal is often (much) larger than the range of diffraction across the crystal surface. Hence effects in on-circle or in-circle geometries should be *insensitive* to a finite source length alone but, particularly in the in-circle case, coupling with a large crystal length can

lead to a large and negative mean off-axis shift to lower apparent angles, given roughly by

$$\frac{\Delta\lambda}{\lambda} \simeq \frac{-1}{24}\left(\frac{y_0^2}{(2R_z)^2 \sin^2\theta_{Ax}} - \frac{\Delta\theta_w^2}{4}\right). \tag{20}$$

K. Crystal and source heights normal to the generatrix

The effects of crystal or source height, independently, result in detected locations off the generatrix, so that quoted shifts[37,40] assume no detector resolution in the transverse direction. These formulas treated the average image location projected onto the generatrix, corresponding to a one-dimensional detector with a large transverse height (and with the source on the Rowland circle). With good two-dimensional detectors and a finite crystal height, but a negligible source height (or, theoretically, a finite source height with a negligible crystal height), there would be no mean shift of the profile on the generatrix from this source.

Once again, these two dimensions are coupled, so that if the crystal and source widths in the transverse direction are both significant, the centroid in the central detector region shall be shifted as follows:

$$\frac{\Delta\lambda}{\lambda} \simeq \frac{h_1^2}{24BX^2}, \tag{21a}$$

$$\Delta Y \simeq \frac{h_1^2(2R_z)\sin\theta_P}{24BX^2 \cos\theta_P}. \tag{21b}$$

For an aligned source and crystal on the Rowland circle ($BX = BP = 2R_z \sin\theta_P$, cf. Fig. 9), this yields the modified standard formula

$$\frac{\Delta\lambda}{\lambda} \simeq \frac{h_1^2}{24(2R_z)^2 \sin^2\theta_P}, \tag{22a}$$

$$\Delta Y \simeq \frac{h_1^2}{24(2R_z)\sin\theta_P \cos\theta_P}, \tag{22b}$$

with an additional contribution due to the detector resolution element, but where

$$h_1 = \begin{cases} \dfrac{h_0 BP}{2R_z \sin\theta_P}, & h_0 \leqslant \dfrac{z_0 2R_z \sin\theta}{2R_z \sin\theta + BP} \\[3mm] \dfrac{z_0 BP}{2R_z \sin\theta_P + BP}, & h_0 > \dfrac{z_0 2R_z \sin\theta}{2R_z \sin\theta + BP} \end{cases} \tag{23}$$

Here h_0 is the crystal height (in the transverse direction) and z_0 is the source height. If the projection of z_0 at the crystal is equal to h_0, a maximum effect occurs which is only 20% of that given by the formulas in Refs 37, 40. The maximum shift for a ray at height h_1 compared to one on the generatrix is 12 times these values (as in the standard formulas).

In the in-circle geometry, this potentially dominant shift is reduced by lateral shifts and the effect of changing curvature on the diffraction profile, asymmetry, and depth penetration. Here the full detailed ray tracing may be expected to reveal such additional shifts, but are of secondary interest in the current exercise.

For the source lying on the Rowland circle, the truncation at low angles and slow dispersion (slow change of diffracting wavelength with position) requires long crystals to image the radiation, adding other shifts, combined with large and negative off-axis shifts to image the peaks back near the original detector location (θ_{min}). The total shift in general has the same sign as in the above expression, but with the magnitude reduced by a factor of 10 or so in typical cases. Once again, this sensitivity to alignment can often preclude precision measurement.

The magnitude of this coupled correction can be several hundred ppm, as indicated above, so this off-axis shift must be allowed for in order to compare wavelengths at or below the level of refractive index corrections. Precision comparisons to calibration lines or calculations are simplified greatly if the crystal width along the generatrix does not limit or truncate the diffraction profile significantly; while adequate resolution in the transverse direction may be assumed to eliminate much of the broadening discussed relating to crystal and source heights h_0 and z_0.

Relative measurements with calibration sources and sources of unknown spectra arising from the same geometric location are able to reduce or allow for the effect of these geometrical shifts arising from finite dimensions. It should be noted that the functional dependence of Eqs. 20–23 are sensitive to the relative magnitudes of diffraction widths, source dimensions, and crystal dimensions. These dependencies are not generally constant functions of angle, so the effects are not canceled by differential measurement. This is particularly true when triangular crystals are used (so that the crystal height can vary with diffracting angle) or when scanning methods adjust the source relative to the Rowland circle (so that θ_{Ax} and θ_P are varied). In addition, the shift of source centers is often significant, and yields potential systematic shifts in the final result which should be considered in subsequent analysis.

L. Secondary corrections

Corrections to the above prescription include the derivation of a mean dy value from estimates of asymmetry with curvature taken into account and the inclusion of extinction accurately and explicitly in Eqs. (10)–(18).

An additional qualitative correction is obtained for (photographic) detectors placed on the Rowland circle. This is also geometric, but depends on absorption coefficients. Such detector shifts in the use of photographic emulsions at non-normal angles can exceed the 10 ppm level. Using the subscript e for the emulsion thickness and attenuation, this yields a simple angular dependence:

$$\Delta Y_z = \left(\frac{\int_0^{t_e/\sin\theta} z e^{-\mu_e z} dz \cos\theta}{\int_0^{t_e/\sin\theta} e^{-\mu_e z} dz} \right)$$

$$= \begin{cases} \dfrac{t_e}{2\tan\theta}, & \mu_e \ll \dfrac{\sin\theta}{t_e}; \\ \dfrac{\cos\theta}{\mu_e}, & \mu_e \gg \dfrac{\sin\theta}{t_e}. \end{cases} \quad (24)$$
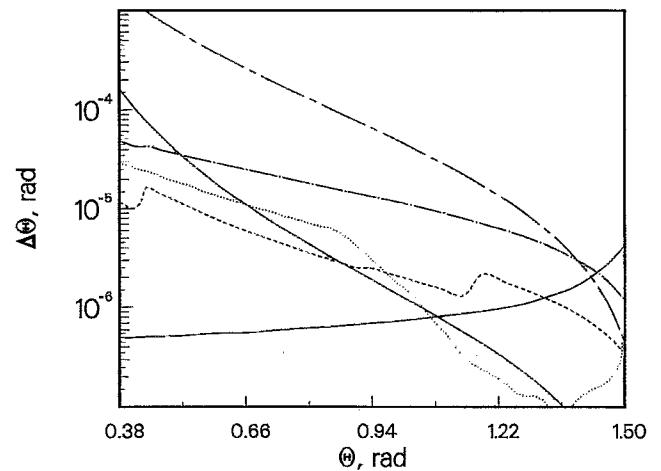

FIG. 16. (a) *Tertiary effects. Emulsion shifts* for PET 002 and PET 008 diffraction and $t_e = 13$ μm assuming $2R_z$ scaling (dashed line and ·–, respectively), compared to the mean shift in diffracting angle for π polarization (dots and slowly increasing solid line) and *maximum lateral shifts* (rapidly decreasing solid line and --). The lateral estimates use Eqs. (16c) and (16d), (14b), (10), and (11a) with μ provided by the absorption coefficient only.

Using a standard thick-emulsion x-ray film with one emulsion removed for higher resolution and assuming $t_e = 13$ μm (cf. Ref. 45) leads to significant relative shifts as indicated in Fig. 16. The emulsion shifts can readily exceed those for lateral detector shifts and mean diffracting angle shifts, in the appropriate regimes. At general angles, all three effects can be important, though often one may be less than a 1% perturbation on the others. Use of electronic or other detectors at normal incidence can eliminate this shift at the expense of off-Rowland circle defocusing.

Mosaicity has small effects on centroid location for curved crystals, defocusing or broadening asymmetric profiles to center more on θ_C than θ_P. The overall asymmetry can significantly affect the centroid determination of experimental profiles, dependent on the fitting function. Doppler broadening and natural linewidths will convolve the asym-
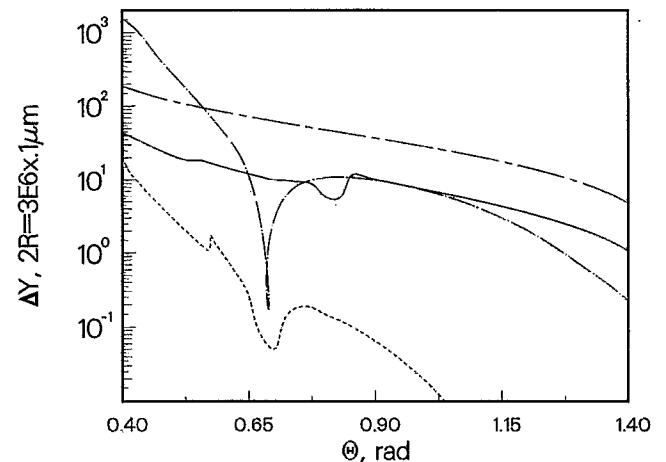

FIG. 16. (b) *Emulsion shifts* for ADP 101 and ADP 404 diffraction (solid line and --, respectively) and $t_e = 13$ μm, compared to the magnitude of lateral shifts from depth penetration (-,·-). Lateral shifts use Eqs. (17b), (18), (10), and (11a), with μ including computed mean extinction for π polarized radiation, and follow the in-circle geometry indicated in Fig. 14.

metry and lead to an uncertainty in centroid determination.

Some of these corrections require evaluation of a (full) dynamical diffraction theory; others require careful ray tracing from the source, inside the crystal, and to the detector. These two requirements are not fully separable. A program has been developed which addresses these corrections in a consistent way and to higher order, including dynamical diffraction theory.[18,19]

Potentially significant effects, not addressed above, are the change of diffraction plane orientation and $2d$ spacing, and hence the diffracting angle, as a consequence of the curvature stress, which may vary with position on the crystal. There is often additional longitudinal and transverse curvature as a result of the bending technique and moments and the isotropic or anisotropic compliances or elasticities of the crystal. Such curvature will give effects in the finite source and crystal height and length considerations of previous sections. It also leads to curvature of the diffracting planes, and hence changes with depth of the orientation of an incident x ray to these planes. This has been addressed above, within the assumption that the planes remain at a constant angle to arcs from the axis of the cylinder. For symmetric Bragg reflection this is exact, while for symmetric Laue diffraction it is true for isotropic materials. In other cases this assumption has limitations leading to tertiary effects in near-symmetric diffraction.

The impressed curvature results in compression of the lateral spacing of the front surface layers and an expansion of lateral spacing of the rear surface, but also gives a variation of lattice spacing normal to the surface (following Poisson's ratio $\nu \simeq 0.25$). This can have a large effect on diffracting angles at the surface compared to the neutral plane at the center of the crystal (equivalent to the unstressed crystal) and can further reduce the range of depths over which diffraction is coherent.[17-19] Form factors can also be redistributed as a result of these stresses. The last two effects are usually minor. Given allowance for the surface d spacing (a potentially large shift to lower angles, but a constant offset in $\Delta\lambda/\lambda$ for all source lines), this change of effective Bragg angle with depth leads to a mean diffracting angle shift proportional to the mean depth $\bar{d}$ and positive for near-symmetric Bragg reflection:

$$\Delta\theta \simeq \nu \tan\theta \frac{\bar{d}}{2R}. \tag{25}$$

For low order diffraction or low energy x rays, this is often negligible, but for intermediate energies can reach $\Delta\lambda/\lambda \simeq 1-5 \times 10^{-6}$, or greater. The shift is zero for plastic deformation as is common with formed mountings for impressing curvature, or for highly mosaic crystals which would also tend to deform plastically. The value and functional form in the elastic case is also dependent upon the crystal shape and stress distribution. This issue is discussed in greater detail in Refs 46 and 47. In symmetric Bragg diffraction, these effects are often tertiary or negligible with respect to the contributions discussed earlier.

M. Discussion

Experiments using curved crystals and requiring absolute wavelength determination to better than 100 ppm in the x-ray regime must generally involve careful consideration of a wide variety of effects in addition to refractive index corrections. Flat crystal modifications to simple estimates of refractive index corrections have been discussed in Sec. II (asymmetric Bragg diffraction, profile asymmetry, three-beam interactions), and are also relevant here. While they can be significant or dominant compared to the refractive index correction itself, even for curved crystals, these contributions are relatively straightforward. Variation of angular shifts with Bragg angle can follow $\tan\theta$, $\cot\theta$, or θ independent relations, with particularly strong local features and alternate dependencies near edges or near three-beam diffraction points.

For most curved crystal geometries, additional systematics in the diffraction process occur at or above this level. Asymmetries of diffraction profiles due to penetration of the x-ray field inside curved crystals can dominate over the refractive index corrections, particularly for high-order diffraction or medium-energy x rays. The shift of the mean angle to the diffracting planes and the lateral shift around the crystal surface of the exit location relative to the incident location of the photon are related and significant, but are often smaller contributions, at the 10%–20% level of the refractive index corrections. Contributions to the mean output angle at the crystal surface can give $\cot\theta$ or $\cos\theta/\sin^3\theta$ dependencies, but often lead to intermediate behavior with complexities from edges, polarizations and $\cos 2\theta$ factors, and geometric considerations. These effects are correlated with Johann aberrations, involving off-axis shifts and potentially large scaling corrections, especially for geometries with the source lying on the Rowland circle or near the minimum angle of the curved crystal spectrometer.

For precision experiments, on-circle geometries should be avoided to minimize arbitrary and sensitive profile truncation shifts from crystal ranges or minimum grazing angles, and to avoid extreme scaling corrections. Geometries with the source well inside the Rowland circle are generally more appropriate for absolute angle measurement or for comparison to suitable calibration lines, due to the greater bandpass and smoother, smaller scaling corrections. Hence nonideal Johann arrangements can provide improved measurements compared to the on-circle ideal. In either case, these off-axis shifts and nonlinearities exhibit strong and rapidly varying angular dependencies, which distort the results given earlier. However, simple functional relations are provided and illustrated for these effects. These indicate angular dependencies for interpolation or extrapolation purposes with regard to calibration lines, and are often accurate to a few percent of the effect or of refractive index contributions. The lowest precision for individual, smaller contributions are typically within a factor of 2 or 3.

Source and crystal dimensions interact with defocusing shifts and diffraction corrections. Literature results often involve restrictive or inappropriate assumptions, and can neglect corrections of large magnitude. Current results indicate that one-dimensional extensions often yield null shifts, but that large shifts can arise from the coupling of two finite dimensions. Relations are also provided for these contributions. The magnitudes and significance vary greatly from on-

circle to in-circle geometries, and tend to recommend the latter. The combination of significant source and crystal dimensions along the generatrix can lead to significant on-circle shifts but quite large (and well-defined) in-circle corrections. This is also true for significant source and crystal heights normal to the generatrix. Dependencies approximating $1/\sin^2 \theta$ can be obtained for these effects, in appropriate regimes, and with significant offsets as discussed above.

Ideally the crystal width along the generatrix should not limit or truncate the diffraction profile significantly, thereby avoiding a strong dependence upon source and crystal geometry and alignment. Adequate resolution in the transverse direction can minimize the effects of crystal and source heights. Centroid shifts due to detectors lying on the Rowland circle (or at general angles to incident x rays) can be significant. The precision of profile shifts can be limited at 0.1%–1.0% of the refractive index corrections by form factor uncertainties, in optimum cases.

Measurements of unknown wavelengths relative to a nearby calibration line by extrapolation can increase the final measurement precision by an order of magnitude, but require an understanding of the functional relations indicated above for higher precision. This can be estimated to first order by the slope of response between several calibration lines. Precision of absolute shifts assumes that relative measurements are made in the same order and with nearby Bragg angles, away from absorption edges and away from extreme spectrometer angles. Multiple-beam interactions are generally not determined or accounted for in such calibrations. If the azimuthal angle is inadequately known, other methods must be used to consider the importance of these effects, as indicated earlier.

The variation with angle of several component effects is often far from constant or linear, so problematic regimes should be avoided, or expected functional dependencies and relative magnitudes should be understood. The series of shifts due to finite source and crystal dimensions are generally more serious for such relative measurements, since different off-axis shifts may arise for the different sources due to their geometric location in space.

Complexity of shifts with order and polarization in spectra necessitates calculations of the sort indicated here for precision below 1% of refractive index corrections. Curved crystal profiles require lamellar thicknesses defined consistently with respect to finite thickness widths and Δy values, allowing for coherence between lamellae, especially for higher order diffraction. The calculated shifts agree well with the sum of simpler estimates, reproducing the dependence on the Bragg angle. The importance of correct allowance for depth penetration and other diffraction effects is also clear.

ACKNOWLEDGMENTS

[1] W. C. Röntgen, Sitzungsberichte der physikalisch-medizinischen Gesellschaft zu Würzburg, December 1895.

[2] M. von Laue, Sitzungber. Math. Phys. Kl. Bayer. Akad. Wiss., Muenchen, 363 (1912).

[3] W. L. Bragg, Proc. Cambridge Philos. Soc. 17, 43 (1913).

[4] See, for example, G. H. Stout and L. H. Jensen, X-Ray Structure Determination A Practical Guide (Macmillan, New York, 1968).

[5] A. Burek, Space Sci. 2, 53 (1976).

[6] C. G. Darwin, Philos. Mag. 27, 315 (1914).

[7] P. P. Ewald, Ann. Phys. 49, 1 (1916); 54, 159 (1917).

[8] J. A. Prins, Z. Phys. 63, 477 (1930).

[9] W. H. Zachariasen, Theory of X-Ray Diffraction in Crystals (Wiley, New York, 1945).

[10] R. W. James, Solid State Phys. 15, 53 (1963).

[11] B. W. Batterman and H. Cole, Rev. Mod. Phys. 36, 681 (1964).

[12] For a recent review of typical instrumentation and modeling, see R. Caciuffo, S. Melone, F. Rustichelli, and A. Boeuf, Phys. Rep. 152, 1 (1987).

[13] A. H. Compton and S. K. Allison, X-Rays in Theory and Experiment (Van Nostrand, Princeton, 1935).

[14] P. P. Ewald, in Advances in X-Ray Spectroscopy, edited by C. Bonnelle and C. Mande (Pergamon, Oxford, 1982) Chap. 11, pp. 202–209; Acta Crystallogr. A 42, 411 (1986).

[15] R. D. Deslattes, E. G. Kessler, W. C. Sauder, and A. Henins, Ann. Phys. NY 129, 378 (1980).

[16] R. D. Deslattes and E. G. Kessler, Jr., IEEE Trans. Inst. Meas. 40, 92 (1991).

[17] C. T. Chantler, D. Phil. thesis, University of Oxford, 1990.

[18] C. T. Chantler, J. Appl. Crystallogr. 25, 674 (1992).

[19] C. T. Chantler, J. Appl. Crystallogr. 25, 694 (1992).

[20] P. J. E. Aldred and M. Hart, Proc. R. Soc. London Ser. A 332, 223 (1973).

[21] D. Eilerman and R. Rudman, Acta Crystallogr. B 35, 2458 (1979).

[22] R. Hall, Ph. D. thesis, University of Leicester, 1980.

[23] A. A. Khan and W. H. Baur, Acta Crystallogr. B 29, 2721 (1973).

[24] L. Tenzer, B. C. Frazer, and R. Pepinski, Acta Crystallogr. 11, 505 (1958).

[25] A. Caticha, Phys. Rev. B 47, 76 (1993).

[26] J. H. Beaumont and M. Hart, J. Phys. E 7, 823 (1974).

[27] M. Deutsch and M. Hart, Phys. Rev. B 26, 5558 (1982).

[28] N. Maskil and M. Deutsch, Phys. Rev. A 37, 2947 (1988).

[29] H. Hashizume, J. Appl. Crystallogr. 16, 420 (1983).

[30] K. Kohra, J. Phys. Soc. Jpn 17, 589 (1962).

[31] J. A. Bearden, J. G. Marzolf, and J. S. Thomsen, Acta Crystallogr. A 24, 295 (1968).

[32] C. T. Chantler, Rad. Phys. Chem. 41, 759 (1993).

[33] C. T. Chantler, in Resonant Anomalous X Ray Scattering. Theory and Applications, edited by G. Materlik, C. J. Sparks, and K. Fischer (Elsevier, North-Holland, Amsterdam, 1994), pp 61–78.

[34] D. Mills and B. W. Batterman, Phys. Rev. B 22, 2887 (1980).

[35] H. J. Juretschke, Acta Crystallogr. A 40, 379 (1984).

[36] Q. Shen, Acta Crystallogr. A 42, 525 (1986).

[37] H. F. Beyer and D. Liesen, Nucl. Instrum. Methods A 272, 895 (1988).

[38] J. M. Laming, D. Phil. thesis, University of Oxford, 1988.

[39] H. F. Beyer, P. Indelicato, K. D. Finlayson, D. Liesen, and R. D. Deslattes, Phys. Rev. A 43, 223 (1991).

[40] G. Zschornak, G. Müller, and G. Musiol, Nucl. Instrum. Methods 200, 481 (1982).

[41] J. Dunn, Ph.D. thesis, University of Leicester, 1990, p. 39.

[42] W. Schwitz, J. Kern, and R. Lanners, Nucl. Instrum. Methods 154, 105 (1978).

[43] A. K. Freund, Nucl. Instrum. Methods 216, 269 (1983).

[44] P. Suortti and A. K. Freund, Rev. Sci. Instrum. 60, 2579 (1989).

[45] C. T. Chantler, Appl. Opt. 32, 2371; 2398; 2411 (1993).

[46] Z. H. Kalman and S. Weissmann, J. Appl. Crystallogr. 16, 295 (1983).

[47] O. I. Sumbayev and A. I. Smirnov, Nucl. Instrum. Methods 22, 125 (1963).